

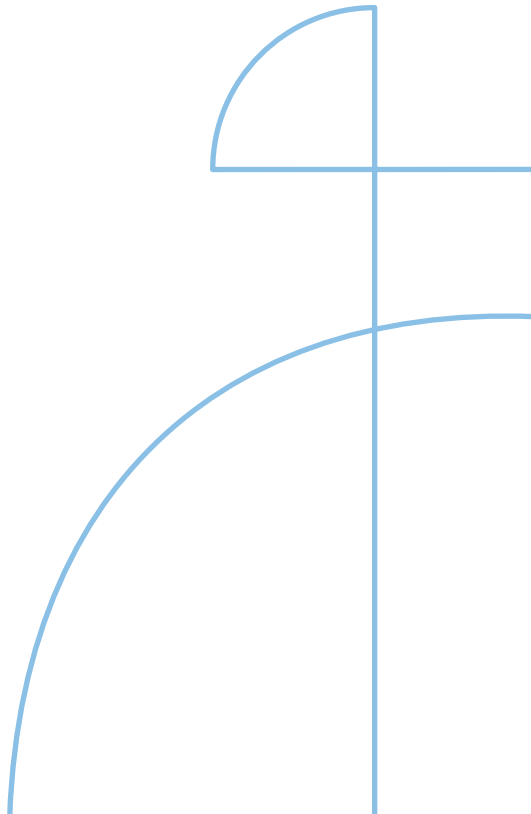


Doctoral Thesis in Materials Science

Catalytic Graphitization of Bio-based Carbon Precursors: A Sustainable Process to Produce Bio-graphite

ZIYI SHI

KTH ROYAL INSTITUTE OF TECHNOLOGY



Catalytic Graphitization of Bio-based Carbon Precursors: A Sustainable Process to Produce Bio-graphite

ZIYI SHI

Academic Dissertation which, with due permission of the KTH Royal Institute of Technology, is submitted for public defence for the Degree of Doctor of Philosophy on Friday the 10th of April 2026, at 9:00 a.m. Kollegiesalen, Brinellvägen 8, Stockholm.

Doctoral Thesis in Materials Science
KTH Royal Institute of Technology
Stockholm, Sweden 2026

© Ziyi Shi

TRITA-ITM-AVL 2026:8
ISBN 978-91-8106-556-5

Printed by: Universitetservice US-AB, Sweden 2026

Abstract

The rapid growth of lithium-ion batteries and electric arc furnace steelmaking has led to a sharp increase in global demand for graphite, while conventional natural and synthetic graphite production routes face critical challenges related to resource security, fossil feedstock dependence, high energy consumption, and environmental impact. This thesis investigates sustainable pathways for producing high-quality graphite from renewable bio-based carbon precursors through catalytic graphitization.

Biochar and pyrolysis bio-oil derived from woody biomass were systematically evaluated as carbon precursors. Laboratory scale catalytic graphitization processes were developed to elucidate the influence of precursor type on graphite yield, crystallinity, microstructure, and reaction pathways. Bio-oil was shown to enable superior graphitic ordering through a gas-solid mediated reconstruction mechanism, while biochar provided substantially higher solid carbon yield, making it more suitable for scalable production.

Key operational parameters influencing catalytic graphitization were then systematically investigated, including catalyst compound, catalyst precursor mixing strategy, graphitization temperature, residence time, catalyst loading amount, and catalyst composition. Nitrate based metal salts exhibited better catalytic efficiency compared with metal powders due to improved dispersion, and wet impregnation significantly enhanced graphitic ordering relative to dry mixing. Elevated temperatures and optimized residence times promoted structural reorganization. Hybrid catalyst systems, particularly trimetallic Fe-Ni-Mn catalysts, demonstrated synergistic effects that significantly improved graphitic crystallinity and microstructural development.

To address scalability limitations and environmental concerns associated with metal salt catalysts, a novel molten metal pool based catalytic graphitization process was developed. Inspired by laboratory observations of a density driven phase separation between molten iron and graphitized carbon, this previously unreported process enables direct high temperature separation of graphite from catalyst without purification. Pilot scale experiments demonstrated semi-continuous production of highly ordered graphite with a minimal residual metal content.

The applicability of the produced bio-graphite was validated in two strategically important applications. In electric arc furnace electrodes, bio-graphite exhibited low electrical resistivity and effective metal melting performance. In lithium-ion batteries, bio-graphite anodes exhibited stable cycling behavior in both half-cell and full-cell configurations. Finally, process simulation and life cycle assessment showed that the proposed biomass-based graphite production pathway achieves substantially lower cumulative energy demand and greenhouse gas emissions compared with conventional natural and fossil derived synthetic graphite routes.

Overall, this thesis establishes a comprehensive framework for sustainable graphite production from bio-based carbon precursors, integrating process development, parameter optimization, scale-up strategy, application validation, and environmental assessment. This work demonstrates that catalytic graphitization is a commercially viable and environmentally superior alternative to conventional graphite supply chains.

Keywords

Bio-graphite, catalytic graphitization, biochar, bio-oil, molten metal pool, lithium-ion batteries, electric arc furnace, life cycle assessment

Sammanfattning

Den snabba tillväxten av litiumjonbatterier och elektriska ljusbågsugnar inom stålindustrin har lett till en kraftigt ökad global efterfrågan på grafit. Samtidigt står konventionella produktionsvägar för naturlig och syntetisk grafit inför betydande utmaningar kopplade till resursbegränsningar, beroende av fossila råvaror, hög energiförbrukning och negativ miljöpåverkan. Denna avhandling undersöker hållbara processvägar för framställning av högkvalitativ grafit från förnybara biobaserade kolprekursorer genom katalytisk grafitisering.

Biokol och pyrolysolja som härrör från träbaserad biomassa utvärderades systematiskt som kolprekursorer. Laboratiebaserade försök med katalytisk grafitisering genomfördes för att klarlägga hur prekursorernas egenskaper påverkar grafitutbyte, kristallinitet, mikrostruktur och reaktionsmekanismer. Resultaten visar att pyrolysolja möjliggör högre grad av grafitisk ordning genom en gas fastmedierad omstrukturering, medan biokol ger ett avsevärt högre fast kolutbyte och därmed är mer lämpligt för uppskalad produktion.

Centrala driftparametrar som styr den katalytiska grafitiseringen undersöktes därefter systematiskt, inklusive katalysatorns form, blandningsstrategi mellan katalysator och prekursor, grafitiseringstemperatur, uppehållstid, katalysatorhalt samt katalysatorsammansättning. Nitratbaserade metallsalter uppvisade högre katalytisk effektivitet än metallpulver på grund av bättre dispersion, och våtimpregnering visade sig ge avsevärt förbättrad grafitisk ordning jämfört med torrblandning. Förhöjda temperaturer och optimerade uppehållstider främjade strukturell omvandling, medan hybrida katalysatorsystem, särskilt trimetalliska Fe Ni Mn katalysatorer, uppvisade

synergistiska effekter som markant förbättrade grafitens kristallinitet och mikrostrukturella utveckling.

För att hantera skalbarhetsbegränsningar och miljöutmaningar förknippade med metallsaltkatalysatorer utvecklades en ny katalytisk grafitiseringsprocess baserad på ett smält metallbad. Processen, som inspirerades av laboratorieobservationer av densitetsdriven fasuppdelning mellan smält järn och grafitiserat kol, har inte tidigare rapporterats i litteraturen. Den möjliggör direkt separation av grafit från katalysator vid hög temperatur utan behov av syrarensning. Försök i pilotskala visade att processen möjliggör kontinuerlig produktion av högordnad grafit med mycket låg kvarvarande metallhalt.

Den framställda biografitens användbarhet verifierades i två industriellt viktiga tillämpningar. Som elektroder i elektriska ljusbågsugnar uppvisade biografiten låg elektrisk resistivitet och effektiv metallsmältning. Som anodmaterial i litiumjonbatterier visade biografiten god cyklingsstabilitet i både halvcell- och fullcellskonfigurationer. Slutligen visade processimulering i Aspen Plus i kombination med livscykelanalys att den föreslagna biobaserade grafitproduktionsvägen har avsevärt lägre kumulativ energianvändning och växthusgasutsläpp jämfört med konventionella produktionsvägar för naturlig och fossilbaserad syntetisk grafit.

Sammanfattningsvis etablerar denna avhandling ett heltäckande ramverk för hållbar grafitproduktion från biobaserat kol, där processutveckling, parameteroptimering, uppskalningsstrategi och miljöutvärdering integreras. Resultaten visar att katalytisk grafitisering utgör ett industriellt relevant och hållbart alternativ till dagens grafitförsörjningskedjor.

Nyckelord

Biografit, katalytisk grafitisering, biokol, pyrolysolja, smält metallbad, litiumjonbatterier, elektrisk ljusbågsugn, livscykelanalys

Acknowledgments

I would like to express my sincere gratitude to my supervisors, Weihong Yang and Pär Göran Jönsson, for their invaluable guidance, continuous support, and insightful discussions throughout my doctoral studies. Their scientific expertise, thoughtful supervision, and great patience have been essential to the successful completion of my Ph.D. work.

I gratefully acknowledge Energimyndigheten for the financial support (Projects: P2021-00048 and P2024-01681) of my research. I would also like to thank Swerim AB, Uppsala University, Envigas AB, and Nordic-Biographite AB for their valuable cooperation during my research.

I sincerely thank all the co-authors of the papers included in this thesis for their contributions to experimental work, their insightful discussions, and their efforts in preparing the manuscripts.

I am deeply thankful to my colleagues at KTH MSE for providing a friendly, inspiring, and supportive working environment. Their help, discussions, and companionship have greatly enriched my doctoral journey. I would especially like to thank Tong Han for his thorough support, guidance, and mentorship. You opened the gate and led me onto my Ph.D. path; you are always a role model for us to follow. I would also like to especially thank Yanghao Jin for constant and invaluable help throughout my studies, whether in experiments, manuscript preparation, or daily life. Special thanks go to my “big brothers,” Shule Wang and Yuming Wen, who showed me what the academic world is truly like. I will never forget the time we spent together, especially every lunch and dinner (food delivery) we shared. I also thank Hanmin, Samina, Yazhe, Boyang, Rikard, Jose,

Yu-chiao, and Luis for their collaboration and support, which made my time in the group and the unit truly memorable.

My warm and special gratitude goes to my friends: Junyuan Guo & Caroline Yang, Chunyu Zhuang, Yuchi Zhang, Hanmin Yang (again) and Gepeng Yang in Stockholm for bringing balance—through skiing, fishing, golf, and delicious food—and joy to my life during these years.

My deepest gratitude goes to my parents for their unconditional love, support, and belief in me. Their sacrifices and encouragement have been a constant source of strength.

Finally, and most importantly, I thank my wife, Yage Hao, for her endless love, patience, and unwavering support. Her understanding, encouragement, and constant companionship have been my greatest strength and made it possible for me to complete this journey. Love You Forever

Ziyi Shi

Stockholm, Sweden

2026

List of publications

Supplement I

Shi, Z., Wang, Y., Lu, M., Yang, H., Han, T., Kong, X., Kallio, T., Jin, Y., Jönsson, P.G. and Yang, W., 2025. Catalytic graphitization of engineered pyrolysis bio-oil for sustainable graphite and hydrogen Co-production. *Renewable Energy*, p.124149.

Supplement II

Shi, Z., Jin, Y., Han, T., Yang, H., Gond, R., Subasi, Y., Asfaw, H.D., Younesi, R., Jönsson, P.G. and Yang, W., 2024. Bio-based anode material production for lithium-ion batteries through catalytic graphitization of biochar: the deployment of hybrid catalysts. *Scientific Reports*, 14(1), p.3966.

Supplement III

Shi, Z., Wang, S., Jin, Y., Zhao, L., Chen, S., Yang, H., Cui, Y., Svanberg, R., Tang, C., Jiang, J. and Yang, W., 2023. Establishment of green graphite industry: Graphite from biomass and its various applications. *SusMat*, 3(3), pp.402-415.

Supplement IV

Shi, Z., Yang, Z., Jin, Y., Yang, H., Wang, Y., Tang, B., Chen, S., Jönsson, P.G., Yang, W. and Tong, H., "Environmentally friendly valorization of biowaste into high-quality battery graphite within molten metal pool." Under review.

Contribution statement

In Supplements I, II, III, IV: Conceptualisation, methodology, software, validation, formal analysis, investigation, resources, data curation, writing-original draft, writing-review & editing, visualization.

List of publications (not included in the Thesis)

Conference:

1. 2025 the 14th International Conference on Material Science and Engineering Technology, Osaka, Japan. Presentation: Transforming Biochar into High-Quality Graphite through Molten Metal Pool.
2. 2025 the International Congress on Battery Materials and Devices, Suzhou, China. Presentation: 'Sustainable Anode Graphite Materials from Pyrolysis Biochar via Catalytic Graphitization Pathways.
3. 2022 Clearwater Clean Energy Conference, Florida, USA. Presentation: Ex-situ catalytic pyrolysis of biomass in fluidized bed reactor to produce high-quality biocrude

Paper:

1. **Shi, Z.**, Liu, S., Wang, S., Niedzwiecki, L., Baranowski, M., Czerep, M., Tang, C., Kawi, S., Wang, C.H., Jiang, J. and Hedenqvist, M.S., 2023. Hydrothermal carbonization coupled with pyrolysis: An innovative approach to digestate management. *Green Energy and Resources*, 1(3), p.100034.
2. **Shi, Z.**, Jin, Y., Svanberg, R., Han, T., Minidis, A.B., Ann-Sofi, K.D., Kjeldsen, C., Jönsson, P.G. and Yang, W., 2023. Continuous catalytic pyrolysis of biomass using a fluidized bed with commercial-ready catalysts for scale-up. *Energy*, 273, p.127288.
3. Jin, Y., Liu, H., Yang, H., Achchige, D.P.S.T., Subasi, Y., Gond, R., Wang, Y., Asfaw, H.D., Chen, S., **Shi, Z. (corresponding author)** and Han, T., 2025. Development of biomass pyrolysis bio-oil as a renewable surface

- engineering agent for bio-based hard carbon production. *Journal of Power Sources*, 641, p.236824.
4. Wang, S., **Shi, Z.**, Jin, Y., Zaini, I.N., Li, Y., Tang, C., Mu, W., Wen, Y., Jiang, J., Jönsson, P.G. and Yang, W., 2022. A machine learning model to predict the pyrolytic kinetics of different types of feedstocks. *Energy Conversion and Management*, 260, p.115613.
 5. Jin, Y., **Shi, Z.**, Han, T., Yang, H., Asfaw, H.D., Gond, R., Younesi, R., Jönsson, P.G. and Yang, W., 2023. From waste biomass to hard carbon anodes: predicting the relationship between biomass processing parameters and performance of hard carbons in sodium-ion batteries. *Processes*, 11(3), p.764.
 6. Jin, Y., Liu, S., **Shi, Z.**, Wang, S., Wen, Y., Zaini, I.N., Tang, C., Hedenqvist, M.S., Lu, X., Kawi, S. and Wang, C.H., 2024. A novel three-stage ex-situ catalytic pyrolysis process for improved bio-oil yield and quality from lignocellulosic biomass. *Energy*, 295, p.131029.
 7. Wang, S., Wang, Y., **Shi, Z.**, Sun, K., Wen, Y., Niedzwiecki, L., Pan, R., Xu, Y., Zaini, I.N., Jagodzińska, K. and Aragon-Briceno, C., 2023. Van Krevelen diagrams based on machine learning visualize feedstock-product relationships in thermal conversion processes. *Communications Chemistry*, 6(1), p.273.
 8. Wang, S., Wen, Y., **Shi, Z.**, Zaini, I.N., Jönsson, P.G. and Yang, W., 2022. Novel carbon-negative methane production via integrating anaerobic digestion and pyrolysis of organic fraction of municipal solid waste. *Energy Conversion and Management*, 252, p.115042.
 9. Yang, H., Han, T., **Shi, Z.**, Sun, Y., Jiang, J., Sandström, L., Jönsson, P.G. and Yang, W., 2022. In situ catalytic fast pyrolysis of lignin over biochar and activated carbon derived from the identical process. *Fuel processing technology*, 227, p.107103.
 10. Wang, S., Wen, Y., **Shi, Z.**, Niedzwiecki, L., Baranowski, M., Czerep, M., Mu, W., Kruczek, H.P., Jönsson, P.G. and Yang, W., 2022. Effect of hydrothermal carbonization pretreatment on the pyrolysis behavior of the digestate of agricultural waste: a view on kinetics and thermodynamics. *Chemical Engineering Journal*, 431, p.133881.
 11. Wen, Y., Wang, S., **Shi, Z.**, Jin, Y., Thomas, J.B., Azzi, E.S., Franzén, D., Gröndahl, F., Martin, A., Tang, C. and Mu, W., 2022. Pyrolysis of engineered beach-cast seaweed: performances and life cycle assessment. *Water Research*, 222, p.118875.

List of abbreviations

LIB	Lithium-ion Battery
EVs	Electric Vehicles
EAF	Electric Arc Furnace
GHG	Greenhouse Gas
LCA	Life Cycle Assessment
IEA	International Energy Agency
SDGs	Sustainable Development Goals
GWP	Global Warming Potential
HF	Hydrofluoric Acid
Lc	Stacking Height
La	Crystallite Size
BET	Brunauer-Emmett-Teller
XRD	X-ray Diffraction
G%	Degree of Graphitization
XPS	X-ray Photoelectron Spectroscopy
TGA	Thermogravimetric Analysis
ICP	Inductively Coupled Plasma

TEM	Transmission Electron Microscopy
SEM	Scanning Electron Microscopy
FTIR	Fourier Transform Infrared Spectroscopy
CHP	Combined Heat and Power
GC	Gas Chromatography
MS	Mass Spectrometry
LCI	Life Cycle Inventory
FWHM	Full Width at Half Maximum
SAED	Selected Area Electron Diffraction
ICE	Initial Coulombic Efficiency
SEI	Solid Electrolyte Interphase
LFP	Lithium Iron Phosphate
CED	Cumulative Energy Demand

CONTENTS

1	Introduction	1
1.1	Introduction	1
1.2	Objectives	3
1.3	Structure of the thesis	6
1.4	Sustainability aspects of the thesis	7
2	Background	9
2.1	Graphite	10
2.2	Catalytic graphitization	11
2.3	Carbon precursors	13
2.4	Parameters of catalytic graphitization	14
2.5	Reactors of catalytic graphitization	15
2.6	Environmental impact of graphite production	16
3	Materials and methods	19
3.1	Carbon precursors	19
3.1.1	Biochar	19
3.1.2	Bio-oil	20
3.2	Catalysts and acid chemicals	20
3.3	Experimental facilities	21
3.3.1	Horizontal electric resistance furnace for catalytic graphitization	21
3.3.2	Induction furnace for catalytic graphitization	21
3.4	Characterization methods and facilities	23
3.4.1	Characterization methods of solid materials	23
3.4.2	Characterization methods of liquid materials	24
3.4.3	Characterization methods of gaseous materials	25
3.5	Application methods	25
3.5.1	Electrode preparation and cycling for electrochemical properties	25
3.5.2	EAF electrode preparation and metal melting tests	25
3.6	Process modelling and life cycle assessment	27
3.6.1	Process modelling	27
3.6.2	Life cycle assessment	29
4	Development of catalytic graphitization processes	31
4.1	Background and aim	31
4.2	Results of lab-scale experiments	33
4.2.1	Characterization of the bio-oil precursor	33

4.2.2	Graphite yield and mass balance	34
4.2.3	Crystallinity and graphitic ordering.....	34
4.2.4	Morphology and microstructural evolution	37
4.2.5	Gaseous coproducts and graphitization pathways	38
4.3	Summary	39
5	Parameter study of catalytic graphitization	41
5.1	Background and aim	41
5.2	Results of lab-scale experiments	42
5.2.1	Effect of catalyst compound	42
5.2.2	Effect of catalyst-precursor mixing strategy.....	44
5.2.3	Effect of graphitization temperature	45
5.2.4	Effect of residence time	48
5.2.5	Effect of catalyst loading amount	51
5.2.6	Effect of single-, bimetallic-, and trimetallic catalysts.....	52
5.3	Application validation	57
5.3.1	Performance as EAF electrode material	57
5.3.2	Electrochemical performance as LIB anode material	58
5.4	Summary	60
6	Scaling up the process by applying molten pool.....	63
6.1	Background and aim	63
6.2	Results of lab-scale experiments	64
6.2.1	Characterization of graphite	64
6.2.2	Physical separation behavior and catalyst redistribution	66
6.3	Results of pilot-scale experiments	68
6.3.1	Characterization of graphite collected at different reaction times	69
6.3.2	Application of the graphite in half-cell and full-cell Li-ion battery	71
6.4	Summary	73
7	Process simulation and life cycle assessment	75
7.1	Process simulation	75
7.2	Environmental impact assessment	76
8	Conclusions and recommendations for future work.....	79
8.1	Overall conclusions	79
8.2	Recommendations for future work.....	82
References	85

1 Introduction

1.1 Introduction

The accelerating transition toward renewable energy systems has generated an unprecedented demand for high-performance carbon materials. Among these, graphite plays a critical role due to its unique structural, electrical, and thermal properties [1]. Graphite, as the predominant anode material in lithium-ion batteries (LIBs), is indispensable in applications such as portable electronics, electric vehicles (EVs), and grid-scale energy storage [2, 3]. With global LIB manufacturing capacity projected to exceed 3000 GWh by 2030, the corresponding demand for graphite is expected to rise dramatically [4]. In addition to the energy storage sector, graphite is used as a critical material in high-temperature metallurgical industries, particularly in electric arc furnace (EAF) steelmaking [5]. Graphite electrodes serve as conductive elements that sustain extremely high temperatures during steel production, with approximately 2 to 4 kg of graphite consumed per ton of steel produced [6]. Globally, the graphite demand for EAF-based steel production has increased to 850,000 tons in 2024 [7]. These numbers indicate that, with the growing worldwide adoption of EAF steelmaking and LIBs development, the demand for graphite continues to rise.

Commercial graphite can be classified into two major categories based on its production route: natural graphite and synthetic graphite. Natural graphite, extracted directly from mining deposits, has been designated as a critical raw material by the European Union due to its high economic importance and significant supply risks [8]. However, its production involves mining, beneficiation, and purification, all of which pose environmental challenges [9].

Specifically, mining operations generate dust, tailings, and hazardous wastewater, while purification often relies on hydrofluoric acid (HF), raising serious ecological and human health concerns. Synthetic graphite is commonly produced from petroleum coke, coal tar pitch, and other fossil-based precursors at temperatures approaching 3000 °C, resulting in substantial greenhouse gas (GHG) emissions and energy consumption [10]. Thus, the growing reliance on graphite for energy storage conflicts with global targets for carbon neutrality and resource sustainability.

To alleviate these supply pressures and environmental burdens, renewable biomass has emerged as a promising alternative carbon precursor. In particular, biomass-derived products offer unique advantages due to its renewability, abundance, and high fixed-carbon content as obtained through pyrolysis [11, 12]. Several studies have demonstrated the feasibility of converting various lignocellulosic feedstocks, such as sawdust, agricultural residues, and forestry byproducts, into functional carbon materials [13]. However, without catalytic assistance, the graphitization of biochar still results in limited structural ordering compared to commercial graphite [14]. This constraint has driven increasing interest in catalytic graphitization, where transition metals, such as Fe, Ni, Co, and Mn, can facilitate carbon dissolution-precipitation/formation-decomposition processes, enabling graphitic layer formation at substantially lower temperatures [15]. Experimental works have confirmed the catalytic activity of these metals and demonstrated the potential to achieve graphite-like structures in renewable precursors at temperatures of 900-1600 °C [16, 17]. This approach significantly reduces energy consumption compared to the production of traditional natural and synthetic graphite.

To move toward practical implementation of catalytic graphitization, this thesis systematically investigates the entire process from the selection of carbon precursor to catalyst design, operational parameters, and the performance of the resulting bio-based graphite (bio-graphite) in targeted applications, as shown in **Figure 1.1**. Building upon these fundamental insights, a novel scalable catalytic graphitization process is proposed and developed. Finally, by integrating laboratory data, process simulation and life cycle assessment (LCA) are carried out to evaluate the environmental impacts across the full bio-graphite value chain, enabling a robust comparison between catalytic graphitization pathways and conventional fossil-based graphite production.

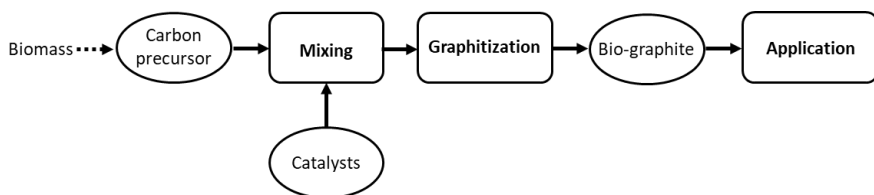


Figure 1.1: The overall process of catalytic graphitization.

1.2 Objectives

The primary aim of this doctoral thesis is to establish, develop, and evaluate pathways for producing bio-graphite from renewable biomass-derived carbon precursors through catalytic graphitization. To accomplish this aim, this research is structured around four interconnected objectives, each corresponding to specific knowledge gaps in catalytic graphitization and following the sequential investigative workflow outlined below:

- Develop catalytic graphitization processes for biomass-derived carbon precursors, including evaluating renewable carbon precursors to establish a feasible method for producing bio-graphite. (Supplement I)
- Investigate key operational parameters and catalyst systems to optimize graphitization performance, including assessing the effects of operating conditions, comparing single-metal, bimetallic, and trimetallic hybrid catalysts, and validating the use of bio-graphite as an anode material for lithium batteries and as an electrode for EAF applications. (Supplement II and III)
- Formulate scalable production strategies as an industrially viable approach and demonstrate industrial feasibility through pilot-scale experiments. (Supplement IV)
- Assess the environmental performance of the catalytic graphitization process and benchmark biomass-derived graphite against conventional fossil-based graphite production routes. (Supplement III)

These objectives are addressed through the systematic methodology illustrated in **Figure 1.2**. This thesis establishes a comprehensive research framework that spans laboratory-scale fundamentals, industrial scale-up, and system evaluations, facilitating the development of sustainable graphite materials for two of the world's most critical industrial sectors.

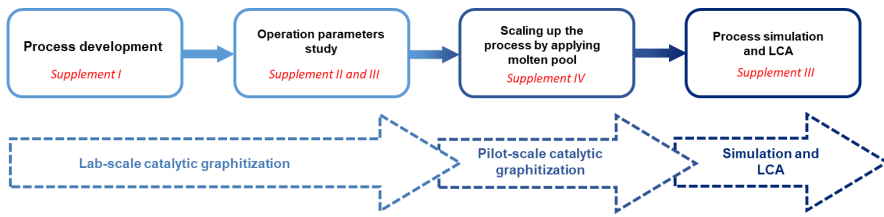


Figure 1.2: The objectives of the thesis.

Table 1.1: Overview of the objective, approach, catalyst and feedstock of each Supplement included in the thesis work.

Supplement	Objective	Approach	Feedstock and catalysts
I	Catalytic graphitization of engineered pyrolysis bio-oil for sustainable graphite and hydrogen co-production	Investigate the potential of pyrolysis bio-oil as carbon precursor for catalytic graphitization and compare the produced bio-graphite with biochar-derived bio-graphite	Lab-scale catalytic graphitization experiments Feedstock: commercial biochar powders and commercial pyrolysis bio-oil. Catalyst: iron powder
II	Bio-based anode material production for lithium-ion batteries through catalytic graphitization of biochar: the deployment of hybrid catalysts	Develop a novel trimetallic catalyst for catalytic graphitization to improve graphitic crystallinity and LIBs electrochemical performance	Lab-scale catalytic graphitization experiments Feedstock: commercial biochar powders. Catalyst: ferric nitrate hexahydrate, bimetallic catalyst, and trimetallic catalyst
III	Establishment of green graphite industry: Graphite from biomass and its various applications	Identify the key operational parameters for catalytic graphitization, demonstrate the applicability of bio-graphite for LIBs anodes and electrodes, and evaluate environmental performance	Lab-scale catalytic graphitization experiments, Aspen simulation and life cycle assessment Feedstock: commercial biochar powders. Catalyst: iron powder and ferric nitrate hexahydrate
IV	Environmentally friendly valorization of biowaste into high-quality battery graphite within molten metal pool	Optimize the catalytic graphitization process, improve the graphite quality, and develop a new process to enable a semi-continuous production with less acid consumption	Lab-scale catalytic graphitization experiments and pilot-scale continuous catalytic graphitization experiments Feedstock: commercial biochar powders. Catalyst: iron powder

1.3 Structure of the thesis

This thesis is organized into eight chapters, following the logical progression from experimental fundamentals and pilot-scale development to system evaluation:

Chapter 1 presents an introduction to the thesis, including its main objectives, overall structure, and sustainability aspects.

Chapter 2 provides a concise overview of graphite and catalytic graphitization. It introduces current graphite production routes, major limitations, the mechanisms of catalytic graphitization, carbon precursors, catalyst systems, reactor configurations, and other relevant foundations.

Chapter 3 describes the materials and methods used in experiments, including the origin of carbon precursors, catalyst preparation procedures, catalytic graphitization setups, configurations of molten metal pool, analytical approaches, simulation and LCA methodology.

Chapter 4 develops catalytic graphitization processes using biomass-derived biochar and bio-oil for graphite production. The aim is to validate the feasibility of producing bio-graphite from biomass-derived feedstocks while providing a comparative analysis of different carbon precursors. This chapter is based on Supplement I.

Chapter 5 investigates and identifies key operational parameters, including temperature, residence time, catalyst loading amount, and catalyst-precursor mixing strategies. It evaluates the performance of single-metal, bimetallic, and trimetallic catalysts to optimize graphitic crystallinity. Furthermore, the chapter demonstrates the practical application of the resulting bio-graphite, with a focus on lithium-ion battery anodes and EAF electrodes. This chapter is based on Supplement II and Supplement III.

Chapter 6 investigates the scale-up potential of catalytic graphitization by introducing a molten metal pool reactor concept, directly inspired by laboratory-scale fundamental studies. A pilot-scale experiment is conducted to verify the feasibility of large-scale production of high-quality bio-graphite. This chapter is based on Supplement IV.

Chapter 7 evaluates the energy consumption and GHG emission of catalytic graphitization process using Aspen Plus process simulation and LCA. Utilizing primary data from the laboratory-scale experiments detailed in Chapter 5, this

analysis quantifies the environmental performance of the proposed pathways. The chapter is based on Supplement III.

Chapter 8 summarizes the main conclusions derived from the combined studies and provides recommendations for future research and development.

An overview of the supplement's contents is shown in **Table 1.1**.

1.4 Sustainability aspects of the thesis

This thesis directly contributes to global efforts toward sustainable and circular carbon material supply chains. Producing graphite from renewable biomass supports several United Nations Sustainable Development Goals (SDGs), particularly in areas related to clean energy, sustainable industry, and climate action.

SDG 7: Affordable and Clean Energy

Bio-graphite enables low-carbon anodes for LIBs, improving the sustainability of renewable energy storage systems.

SDG 9: Industry, Innovation and Infrastructure

Developing catalytic and molten-metal-assisted graphitization pathways stimulates innovation in critical material supply chains for both battery and steel industries.

SDG 12: Responsible Consumption and Production

Valorizing biomass residues into graphite promotes circularity, reduces dependence on fossil resources, and aligns with sustainable production principles.

SDG 11: Sustainable Cities and Communities and SDG 13: Climate Action

Lower-emission graphite production contributes to decarbonizing both LIB manufacturing and EAF steelmaking, which are two pillars of future low-carbon infrastructures.

Through the integration of process design, sustainability evaluation, and industrial scale-up strategies, this thesis advances holistic approaches for transitioning to sustainable graphite production that can serve multiple critical applications.

2 Background

Graphite is an essential industrial carbon material with applications including energy storage, metallurgy, refractories, lubricants, sealing systems, and advanced composite materials [18]. Among these, its two most critical uses today are anodes in LIBs and consumable electrodes in EAFs [19]. These applications highlight the strategic importance of graphite in modern low-carbon infrastructures. In LIBs, graphite is the preferred anode material because of its favorable lithiation properties, good theoretical capacity (372 mAh g^{-1}) [20], chemical stability, and comparatively low cost (approximately \$8-\$13 per kilogram) [21]. It typically accounts for 15-30% of a lithium-ion cell's mass [22]. According to projections by the International Energy Agency (IEA), global graphite demand is expected to increase from approximately 4 million metric tons in 2021 to over 16 million metric tons by 2040, with LIBs accounting for nearly 10 million metric tons of the total demand [23]. In EAF steelmaking, graphite also plays an important role. Approximately 2 to 4 kg of graphite is consumed to produce one metric ton of steel. The demand for EAF graphite electrodes is projected to reach nearly 1.99 million tons by 2030 [6, 24]. These growing demands from the energy storage and steel sectors are expected to give substantial pressure on the global graphite supply chain.

Currently, commercial graphite is produced either from natural mineral deposits or via artificial synthesis, and it is therefore classified as natural graphite or synthetic graphite [25]. Natural graphite production involves a chemical purification which requires hazardous reagents such as HF, leading to serious health and environmental risks [26]. Moreover, natural graphite deposits are geographically concentrated in China which accounts for about 70% of the world's natural graphite production [27]. This geographic imbalance

introduces supply vulnerabilities and geopolitical risks into the global graphite supply chain. Synthetic graphite, widely used in LIB anodes, is produced from fossil fuel-derived precursors such as petroleum coke, or coal-tar pitch. The production process includes high-temperature graphitization (3000 °C) [28]. The production of synthetic graphite not only raise sustainability concerns but also contribute to substantial CO₂ emissions due to the huge energy consumption [29].

Given these concerns, global graphite supply chains face increasing pressure from rapidly growing demand, limited natural reserves, fossil feedstock dependency, and significant environmental impacts. Consequently, the scientific community has intensified efforts to develop renewable carbon sources and sustainable production pathways, particularly catalytic graphitization techniques for producing high-performance graphite suitable for lithium-ion battery anodes and EAF electrodes.

This chapter provides the theoretical and technological background relevant to the development of bio-based synthetic graphite. It introduces the fundamental principles of graphite structure and properties, describes catalytic graphitization mechanisms, discusses carbon precursors and catalyst systems, and outlines life cycle considerations relevant to graphite production.

2.1 Graphite

Graphite, also referred to as black lead, is a crystalline allotrope of carbon characterized by a hexagonal layered structure composed of six-membered rings arranged in parallel sheets with an AB-AB or ABC-ABC stacking sequence [30]. Within each graphene layer, carbon atoms are sp²-hybridized and bonded to three neighboring atoms with a bond length of approximately 0.142 nm, forming a highly stable planar network, as shown in **Figure 2.1**. [31]. The layers are held together by weak van der Waals forces, giving rise to an interlayer spacing of about 0.335 nm and enabling the sheets to slide readily over one another [1]. This anisotropic bonding results in graphite's unique physical properties, including its softness, lubricating behavior, and high electrical and thermal conductivity along the basal planes due to the presence of delocalized π -electrons. Chemically, graphite is relatively inert under ambient conditions but can engage in reactions with strong oxidizing agents or undergo intercalation, in which atoms or molecules insert between layers and tune its structural and electronic characteristics [32].

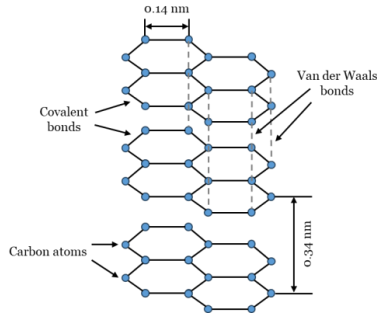


Figure 2.1: Atomic structure of graphite.

Graphite is classified as natural graphite and synthetic graphite. Natural graphite is extracted from selective geological deposits and processed through crushing, flotation, shaping, and purification. In 2021, China accounted for around 70% of the global natural graphite production, while Europe produced only about 2 to 3%, highlighting the strong geographic concentration of supply [33]. Natural graphite typically contains mineral impurities, including quartz, silicates, silicon dioxide, and calcium oxide, which must be removed to meet battery-grade specifications [34]. Industrial purification often relies on hydrofluoric acid, consuming about 0.25 kg of HF per kilogram of purified graphite [35]. This method is both environmentally damaging and hazardous to human health. The dependency on a small number of mining regions further exacerbates supply risk and limits long-term scalability.

Synthetic graphite is produced from petroleum residues (petroleum coke and coal tar pitch) through multiple high-temperature steps, including delayed coking (500 °C), calcination (1200 °C), and graphitization (3000 °C) [36]. Graphitization converts disordered carbon matrices into well-ordered hexagonal graphite through thermally activated atomic rearrangement. The slow production rate, high energy consumption, and reliance on petroleum residues have driven interest in alternative precursors and milder production pathways. Compared with natural graphite, synthetic graphite is more preferable as anodes for LIBs due to its higher uniformity. Approximately 50% of graphite used in LIB anodes currently originates from synthetic graphite, and this percentage is expected to rise to 70% by 2030 [37, 38].

2.2 Catalytic graphitization

As discussed, the growing demand for graphite materials and the pressing requirement for sustainable production routes have intensified interest in

catalytic graphitization as an alternative to traditional high-temperature synthesis. Traditional graphitization requires temperatures up to 3000 °C and fossil fuel-based materials as feedstock. In contrast, catalytic graphitization enables the transformation of non-graphitizable amorphous carbon (like woods) into graphite at significantly lower temperatures (usually lower than 2000 °C) by using metal catalysts [15].

The concept of catalytic graphitization dates back to 1896, when Acheson observed that certain impurities accelerated the conversion of amorphous carbon into graphitic structures at reduced temperatures [39]. Subsequent research has identified two widely accepted mechanisms: dissolution-precipitation mechanism, where carbon dissolves into the molten catalyst and precipitates as graphite, or formation-decomposition mechanism, where carbon forms intermediate carbides that break down into graphite (**Figure 2.2**) [40]. These mechanisms reveal that the catalysts (metals) enhance carbon atom mobility and promote structural reordering at temperatures much lower than those required for traditional graphitization.

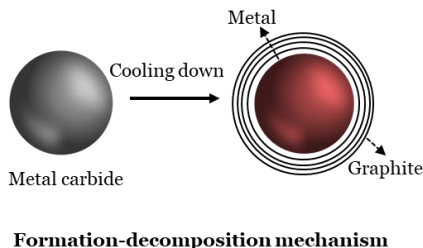
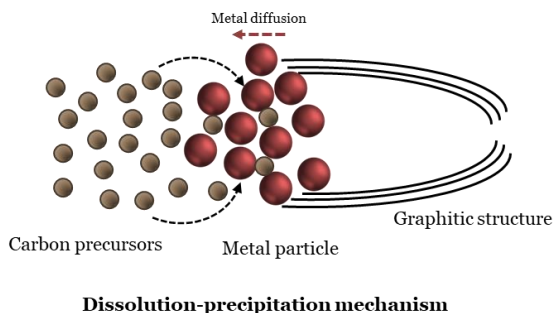


Figure 2.2: The mechanisms of catalytic graphitization.

Over the past decades, more and more studies have been made to investigate catalytic graphitization processes. **Figure 2.3** illustrates the number of graphitization-related papers published in the Web of Science database from 2000 to 2025. During this period, extensive research has been done on parameter studies such as temperature, reaction time, catalyst composition and loading amount [41]. Some studies also highlight the importance of selecting suitable carbon precursors and employing appropriate reactor configurations [42].

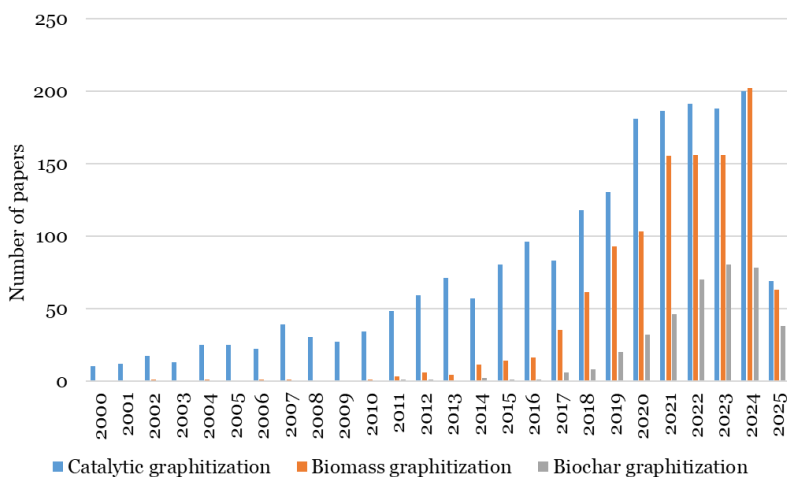


Figure 2.3: Publication statistics of graphitization-related papers in the Web of Science database from 2000 to 2025.

2.3 Carbon precursors

The selection of the carbon precursor is crucial in catalytic graphitization because its composition, structure, and ash content directly affect catalyst–carbon interactions, graphitization efficiency, and the quality of the produced graphite. During the past two decades, a wide range of precursors have been explored, including synthetic polymers, raw biomass, hydrothermal carbon, and biocarbon from pyrolysis. Each precursor presents specific advantages and limitations that determine its suitability for a scalable production.

Synthetic polymers and small organic molecules offer high purity and low ash content, leading to efficient catalyst dispersion and high-quality graphitic products [43, 44]. However, their low carbon yield and high cost make them impractical for large-scale production. Biomass precursors such as cellulose,

lignin, or agricultural residues are renewable and widely available, but their high volatile content, structural heterogeneity, and variable mineral composition can negatively impact graphitization and introduce impurities into the final material [45-47]. Hydrothermal carbon improves the precursor uniformity and reduces certain inorganic impurities, yet its relatively low fixed-carbon content and the release of hazardous volatiles during heating limit its industrial feasibility [48, 49]. In contrast, biocarbon (biochar) produced by pyrolysis at 400-900 °C has emerged as the most promising precursor. Biochar typically contains 60-85% fixed carbon, low volatile content, and a porous microstructure that enhances catalyst accessibility [50]. These characteristics make pyrolysis-derived biochar particularly suitable for catalytic graphitization and a scalable production of bio-graphite.

2.4 Parameters of catalytic graphitization

The efficiency of catalytic graphitization and the quality of the resulting graphite are influenced by a combination of interrelated process parameters. These parameters influence catalyst activity, carbon mobility, reaction pathways, and the development of graphitic crystallinity. Among them, temperature, residence time, catalyst composition, loading amount, and catalyst-precursor mixing strategy are considered the most critical.

Temperature is the dominant parameter controlling catalytic graphitization. In catalytic systems, partial graphitic ordering can occur at temperatures as low as 600 to 800 °C, while well-developed graphite structures are typically achieved between 900 and 1600 °C, depending on catalyst composition and stability [41].

Residence time is also crucial, as it determines how long carbon and the catalyst remain in contact and able to interact. S. Lee et al. verified that long residence times generally promote increased crystallite size and improved structural ordering, but extended exposure at high temperatures may cause catalyst gasification, negatively affecting yield and efficiency [51, 52]. Therefore, an optimal balance between temperature and residence time is required to maximize graphitization while minimizing energy consumption and catalyst degradation.

Catalyst composition and loading significantly affect graphitization behavior. Transition metals such as Fe, Ni, and Co are widely reported as effective catalysts due to their ability to dissolve carbon and facilitate dissolution-precipitation mechanisms [53]. In practice, a variety of catalyst compounds, including metal salts, metal oxides, metal-organic compounds, and non-metal catalysts such as

boron, have been employed to facilitate catalytic graphitization [39]. In addition to catalyst composition, increasing catalyst loading generally enhances graphitization by increasing the number of active sites and improving carbon solubility [54]. Recent studies further demonstrate that bimetallic catalyst systems can exhibit synergistic effects, enhancing catalyst mobility, stabilizing active phases, and promoting more uniform graphite formation compared with single-metal catalysts [55].

The precursor-catalyst mixing strategy is another key parameter. Wet impregnation, and mechanical milling are commonly used approaches, each affecting catalyst dispersion and accessibility [56, 57]. Uniform catalyst distribution enhances carbon dissolution kinetics and promotes homogeneous graphitic growth, whereas poor mixing can result in localized graphitization and heterogeneous product quality.

Overall, catalytic graphitization performance is determined by the combined effects of these parameters rather than any single factor. Understanding and optimizing their interactions is essential for achieving high-quality graphite at reduced temperatures and for developing scalable, energy-efficient production routes suitable for industrial applications.

2.5 Reactors of catalytic graphitization

Reactor configuration is crucial in determining the feasibility, energy efficiency, and scalability of catalytic graphitization processes. While laboratory-scale studies have demonstrated the effectiveness of catalytic graphitization using various carbon precursors and catalysts, translating these findings into industrial-scale production requires reactor systems capable of high-temperature operation, efficient heat transfer, and high-throughput processing.

Conventional laboratory-scale catalytic graphitization is most commonly conducted in electric resistance furnaces due to their simplicity and precise temperature control. However, these furnaces rely on indirect heating, resulting in slow heating rates, high energy losses, and limited scalability. Joule heating systems, in which electrical current passes directly through conductive carbon materials, offer improved energy efficiency and rapid heating but require sufficient electrical conductivity of the precursor, restricting their applicability [58]. Microwave and laser heating approaches provide rapid and localized heating and have demonstrated enhanced graphitization efficiency at reduced energy input [40, 59]. However, their industrial implementation is challenged

by a non-uniform field distribution, a limited penetration depth, and difficulties in scaling reactor size.

Induction furnace is a more industrially relevant option, particularly in the metallurgical industry for melting metals. Induction furnace uses an electromagnetic field to heat materials. The process begins by passing alternating current through a coil, which generates an alternating magnetic field. This magnetic field induces electrical currents, known as eddy currents, within the material, causing it to rapidly heat up due to the material's resistance. This method can also be adapted for some high-temperature processes, such as catalytic graphitization. One of the primary advantages of induction heating is its ability to provide very fast heating rates, and uniform heat distribution within the material. And as heat is generated directly inside the material through eddy currents, there are minimal heat losses compared to traditional methods like electrical resistance furnaces [60]. This makes induction heating highly efficient. In catalytic graphitization, the induction furnace can heat carbon precursors, such as biochar, coal, or other carbon-based materials, to temperatures as high as 3000 °C. For example, X. Zhao et al. used an induction furnace to produce graphite from gasification carbon at 2800 °C [61]. T. Wang et al. employed an induction furnace for catalytic graphitization using H_3BO_3 , La_2O_3 , Pr_6O_{11} , and CeO_2 as catalysts at 2600 °C [62]. Overall, the induction furnace is one of the most promising furnaces to use for large-scale catalytic graphitization. Its ability to reach extremely high temperatures, coupled with its high energy efficiency and scalability, makes it particularly suitable for industrial applications.

2.6 Environmental impact of graphite production

LCA has become an essential tool for evaluating the environmental performance of graphite production, particularly in low-carbon industrial processes. As graphite demand grows rapidly, the environmental impacts of graphite production have attracted increasing attention. **Figure 2.4** displays the energy consumption and GHG emission for natural and synthetic graphite production. For natural graphite, LCA studies typically include mining, beneficiation, purification, and post-processing stages. Based on IPCC 100-yr horizon, the reported global warming potential (GWP) value for natural graphite is approximately 5,316 kg CO_2 -eq/kg-natural graphite. The total energy consumption is 112.5 MJ/kg-natural graphite [63].

Synthetic graphite production also exhibits a substantially high environmental footprint due to its reliance on fossil-derived feedstocks and extremely energy-intensive thermal processing. Q. Dai et al. estimated the energy consumption and GWP values for synthetic graphite production are 89.9 MJ/kg-synthetic graphite and 4.86 CO₂-eq/kg-synthetic graphite [64]. Recent work by D. Surovtseva et al. provides one of the most comprehensive and transparent inventories for synthetic graphite production, demonstrating that many earlier LCAs significantly underestimated impacts by excluding upstream oil refining, coke calcination, and post-processing stages. When these stages are fully accounted for, the GWP value for synthetic graphite is estimated at 13.80 kg CO₂-eq/kg-synthetic graphite [36].

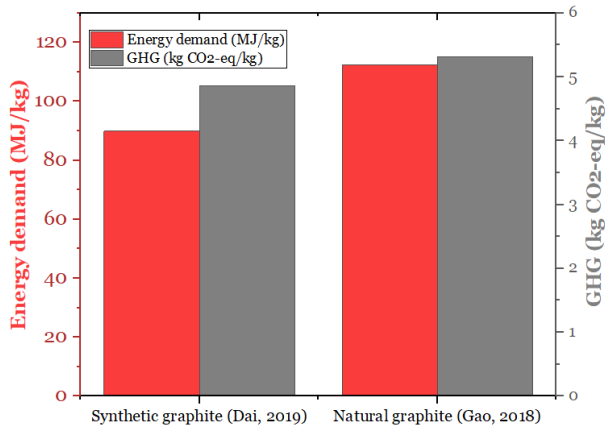


Figure 2.4: The energy consumption and GHG of graphite production in studies.

Given this background, biomass-derived graphite produced via catalytic graphitization represents a promising pathway to reduce environmental impacts while maintaining material performance. Biomass feedstocks offer renewable carbon sources, and catalytic graphitization enables graphitic structure formation at substantially lower temperatures than conventional synthetic routes. Integrating LCA with process modeling tools, such as Aspen Plus, provides a systematic framework to quantify energy consumption, GHG emissions, and trade-offs across laboratory-scale, pilot-scale, and potential industrial-scale systems. Such integrated assessments are essential for benchmarking bio-based graphite against conventional natural and fossil-derived synthetic graphite and for guiding the development of scalable, low-impact graphite production technologies.

3 Materials and methods

3.1 Carbon precursors

3.1.1 Biochar

The biochar used as the carbon precursor in Supplements I-IV was supplied by Envigas AB. A photograph of the biochar is shown in **Figure 3.1**. The biochar was produced via pyrolysis of sawdust at 550 °C. The results of elemental analysis of the biochar are presented in **Table 3.1**.



Figure 3.1: The photograph of biochar materials.

Table 3.1: Elemental analysis of biochar.

Biochar	
Elemental analysis (Wt.%, dry basis)	
C	83.50

H	2.68
N	0.26
S	0.21
O ^a	13.35

^aCalculated by difference.

3.1.2 Bio-oil

The pyrolysis bio-oil used as the carbon precursor in Supplement I was provided by Envigas AB. The pyrolysis bio-oil in this study was obtained from a pyrolysis process of sawdust performed at 550 °C. The results of elemental analysis of the bio-oil are presented in **Table 3.2**.

Table 3.2: Elemental analysis of bio-oil.

	Bio-oil
Elemental analysis (Wt.%, dry basis)	
C	33.49
H	10.14
N	0.16
S	-
O ^a	56.20

^aCalculated by difference.

3.2 Catalysts and acid chemicals

Iron powders (purity > 99%) were employed as catalysts in Supplement I, Supplement III and Supplement IV. And ferric (III) nitrate nonahydrate ($\text{Fe}(\text{NO}_3)_3 \cdot 6\text{H}_2\text{O}$) was used as catalyst in Supplement II and Supplement III. Nickel (II) nitrate hexahydrate and Manganese (II) nitrate were used as catalysts in Supplement II. All the materials were purchased from Sigma Aldrich. Hydrochloric acid (ACS reagent) with 1 mol/L was used as acid chemical for leaching and purchased from Sigma-Aldrich.

3.3 Experimental facilities

3.3.1 Horizontal electric resistance furnace for catalytic graphitization

In Supplementary Materials I, II, and III, laboratory-scale catalytic graphitization experiments were conducted using a horizontal resistance furnace (Kejia Electric Furnace Co., Ltd.). The furnace consists of three independently controlled heating zones, each regulated by a dedicated temperature controller. Real-time sample temperatures were monitored throughout the experiments using K-type thermocouples. Nitrogen was continuously introduced into the furnace tube from the heating phase through the cooling phase to maintain an inert atmosphere. **Figure 3.2** presents a schematic diagram of this horizontal electric furnace.

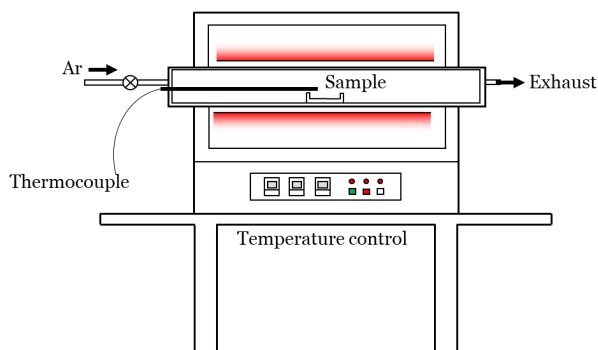


Figure 3.2: The schematic diagram of horizontal furnace at KTH.

3.3.2 Induction furnace for catalytic graphitization

In Supplementary Material IV, laboratory-scale catalytic graphitization was performed using an induction furnace (FMJ 120 F model, SinterCast International Ltd.). The graphite crucible was externally wrapped with refractory bricks to minimize heat loss. Argon gas was employed as the protective atmosphere during graphitization. The crucible temperature was monitored using a Type B thermocouple. **Figure 3.3** presents a schematic diagram of this induction furnace setup.

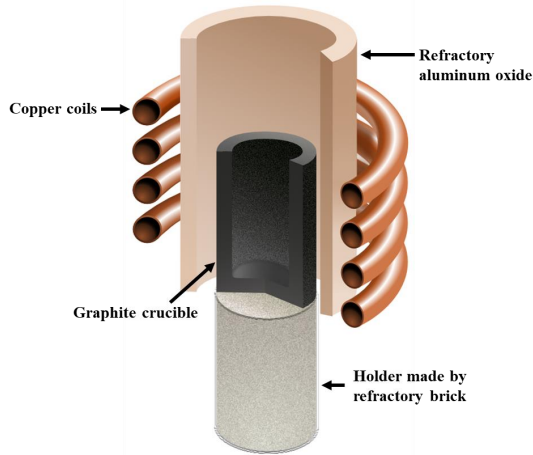


Figure 3.3: The schematic diagram of the induction furnace at KTH [65].

A 75-kW induction furnace (3 kHz, Inductotherm 75 KW, Elkem carbon AB, Norway) was used for pilot-scale catalytic graphitization in Supplement IV. The graphite crucible had a 15-liter capacity (around 90 kg iron). Argon was injected via a gas lance to prevent oxidation. A type B thermocouple was used to measure the crucible temperature. The photographs of the setup are shown in **Figure 3.4**.

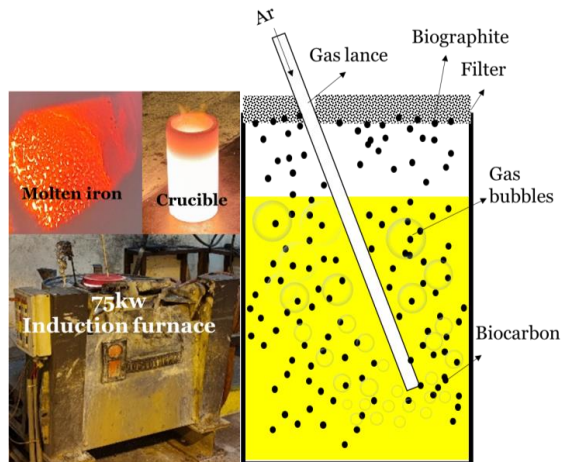


Figure 3.4: Photographs and schematic illustration of the induction furnace for pilot-scale experiments [65].

3.4 Characterization methods and facilities

3.4.1 Characterization methods of solid materials

Crystal information for solid samples was obtained using an X-ray diffractometer (XRD, PANalytical X'Pert Pro) equipped with a Cu K α source (voltage 30 kV, current 15 mA). The Bragg angle scan range was $2\theta = 10^\circ$ to 80° , with a step speed of $0.05^\circ/\text{s}$. The interlayer spacing of the 002 plane was determined by using Bragg's equation [66]:

$$d_{002} = \frac{\lambda}{2\sin\theta} \quad (1)$$

where λ denotes the wavelength of Cu K α , θ is the Bragg angle, and d_{002} refers to the interlayer spacing of the 002 plane.

Based on d_{002} , the degree of graphitization (G%) was determined using the following formula [67]:

$$G\% = \frac{0.3440 - d_{002}}{0.3440 - 0.3354} * 100 \quad (2)$$

The stacking height (L_c) and the crystallite size (L_a) for each sample were determined using the equation below [67]:

$$L_a = \frac{k_1\lambda}{\beta_{(100)}\cos\theta} \quad (3)$$

$$L_c = \frac{k_2\lambda}{\beta_{(002)}\cos\theta} \quad (4)$$

where k denotes the Scherrer constant ($k_1 = 1.84$, $k_2 = 0.94$), $\beta_{(100)}$ and $\beta_{(002)}$ are the angular widths (in radians) of peaks (100) and (002) at half maximum intensities, respectively.

Morphological features were observed using a Hitachi S3700N scanning electron microscope system (SEM), operating using a voltage of 20 kV and working distance of 10 mm. And a Thermo Fisher Scientific Apreo 2s LoVac field emission gun scanning electron microscope. Additionally, an integrated energy dispersive spectroscopy imaging (ChemiSEM) capability was achieved within the SEM software using a Thermo Fisher Scientific Ultradry 60 mm² EDS detector.

The specific surface area was determined using a Micromeritics ASAP 2420 instrument (N₂ adsorption-desorption isotherms at 77 K) and calculated based on the Brunauer-Emmett-Teller (BET) equation [68].

Raman spectra were acquired with a Tyrode I Raman microscope equipped with a 532-nm wavelength diode laser. The degree (α) from disordered carbon to graphitic carbon was calculated as follows:

$$\alpha = \frac{I_G}{I_D} * 100\% \quad (5)$$

where I_G and I_D are the intensities of G band and D band, respectively.

Atomic morphologies were examined by using transmission electron microscopy (TEM). Hitachi TEM HT7700 with the 2k × 2k CCD camera (AMT XR41, USA) was used and operated at 120 kV.

X-ray photoelectron spectroscopy (XPS) was performed with a Kratos Ultra 2 Spectrometer, featuring a 500 mm Rowland circle monochromated Al K α X-ray source, at a vacuum of 5*10⁻⁶ Pa.

The element content of Fe was analyzed by using inductively coupled plasma (ICP) optical emission spectrometry (ICP-OES, Agilent 720).

Thermogravimetric analysis (TGA) was performed on a Mettler TGA/DSC 3+ Stare system. The samples were weighed into 100 μ L Aluminum cups. Dry oxygen gas (50 ml min⁻¹) was flushed during the analysis. The samples were heated from 25 to 900°C at 10 °C min⁻¹.

3.4.2 Characterization methods of liquid materials

Fourier-transform infrared spectroscopy (FTIR, Perkin-Elmer Spectrum 100) was used to determine the chemical composition of liquid samples. The spectral resolution was set to 4 cm⁻¹ and wavelength ranges from 4000 cm⁻¹ to 600 cm⁻¹ was used, with an average of 16 scans.

Liquid samples were analyzed by gas chromatography mass spectrometry (GC MS, Agilent 7890A coupled with Agilent 5975C). Approximately 0.5 g of liquid sample was diluted with 5 mL acetone and 5 mL dichloromethane and mixed until homogeneous. The solution was filtered through a 0.45 μ m syringe filter and transferred to a GC MS vial. Analyses were performed using an HP5 MS column with helium as the carrier gas at a flow rate of 1 mL min⁻¹. The oven was initially held at 40 °C for 1 min, thereafter increased at 3 °C min⁻¹ to 280 °C, and finally maintained for 15 min. A split ratio of 5:1 was applied. Mass spectra were recorded in the range of 45 to 550, and compounds were identified using the NIST 11 library [69].

3.4.3 Characterization methods of gaseous materials

The gases generated during catalytic graphitization were monitored in real-time using a micro-GC (Agilent 490 model). Four columns with thermal conductivity detectors were used to detect N₂, H₂, O₂, CH₄, CO, CO₂ and other small hydrocarbons (C₂-C₄).

3.5 Application methods

3.5.1 Electrode preparation and cycling for electrochemical properties

Electrochemical performance was evaluated using CR2032 coin cells and pouch cells. The detailed half-cell configurations can be found in Supplements I-IV.

Full-cell tests were assembled in CR2032 cells using LiFePO₄ as the cathode and lithiated bio-graphite as the anode (N:P ratio =1.2). Electrodes contained 80 wt% active material, 10 wt% sodium alginate binder, and 10 wt% carbon black, with a mass loading of 1.5-2.0 mg cm⁻². Cells were cycled between 2.7 and 3.9 V using 1 M LiPF₆ in Ethylene Carbonate (EC), Dimethyl Carbonate (DMC), and Ethyl Methyl Carbonate (EMC) (EC:DMC:EMC=1:1:1 vol%) with 1% Vinyl Carbonate as the electrolyte. The rate capability was evaluated from 0.5 C to 5 C after an initial stabilization at 0.2 C.

3.5.2 EAF electrode preparation and metal melting tests

Pyrolysis bio-oil was used as a binder for graphite powder to prepare EAF electrode samples. The bio-oil underwent heat treatment at 80°C in a water bath for 72 hours. Following pretreatment, to prepare the electrode samples, 35% (mass fraction) of the treated pyrolytic bio-oil was premixed with 65% (mass fraction) graphite powder. The mixture was then loaded into a cylindrical mold (alloy tool steel: Cr12MoV) and pressed in a manual hydraulic press. The maximum pressure of the manual hydraulic press was 10 tons. During each test, after the pressing pressure reached its peak, it was maintained for 10 minutes to ensure a complete compaction of the graphite powder. The final compacted product was demolded and placed in a horizontal tube furnace for heat treatment (800°C, 1 hour).

As shown in **Figure 3.5**, a small EAF was constructed using the prepared EAF graphite electrode samples. Graphite electrodes and metal rods were embedded into two copper blocks and connected to the positive and negative terminals of the power source. The power source employed was an ESAB LHH 400 UNIVERSAL welding machine, with a rated output power range of 9 A/20 V to

400 A/36 V. During testing, the device output current was set to 100 A. One electrode was mounted on a track for movement, enabling control of the electrode gap to ensure stable arc generation. The furnace body was fabricated from a hollowed-out single alumina refractory brick, serving both insulation and molten metal storage functions. Electrode melting efficiency was expressed as the mass of graphite electrode consumed per ton of molten metal produced.

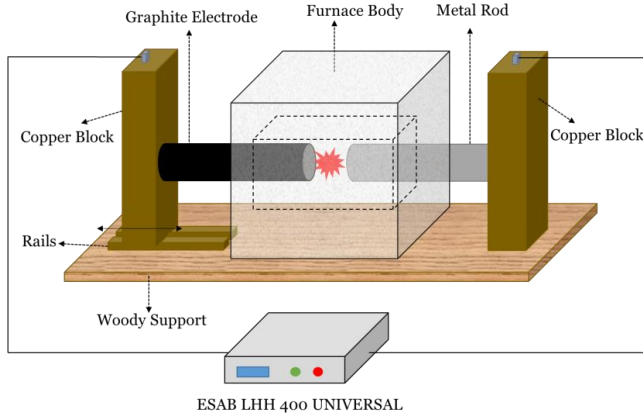


Figure 3.5: A small EAF constructed at KTH [65].

The resistivities of the graphite electrodes were measured by using a four-probe resistivity test system, which consisted of one DH1718E-4 regulated DC power output device and one 199 System DMM/SCANNER. A schematic diagram of the test equipment and the corresponding test principle are shown in **Figure 3.6**. During the measurement, two probes connected to the regulated DC power output device supplied a constant current to the graphite products and two probes connected to the scanner measured the voltage/resistance of the graphite products. The output voltage and current ranges of the DC power output device were 0-30 V and 0-3 A, respectively. A measurable voltage range of the scanner varied between 1×10^{-5} to 200 V. The resistivity of the bulk was further calculated using the following equation:

$$\rho = \frac{V * S}{I * L}, \quad (6)$$

where V is the voltage detected by the scanner, I is the current passing through the bulk, S is the area of the bulk, and L is the length of the bulk.

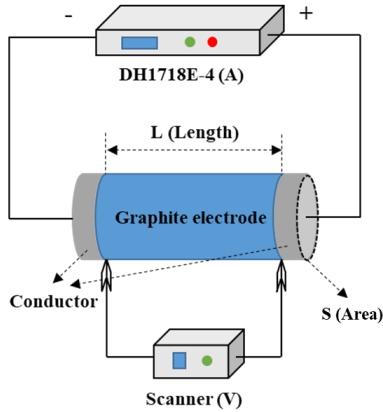


Figure 3.6: A four-probe resistivity test system at KTH [65].

3.6 Process modelling and life cycle assessment

3.6.1 Process modelling

The thermal conversion of biomass into practical graphite products was modeled using Aspen Plus V11.0 based on the results from the experimental section. The detailed environment is presented in **Table 3.3**. The process model included the processes of pyrolysis, catalytic graphitization, and catalyst recycling, as shown in **Figure 3.7**. All the components defined in this simulation are shown in Supplement III.

Table 3.3: Summaries of the simulation environment and basic assumptions of energy efficiency.

Parameters	Value
Base Method	UNIQUAC
Input Mode	Steady state
Ambient pressure	1 atm
Stream class	MIXCINCPD
Energy efficiency of furnace	80%

3.6.1.3 Energy recovery from coproduct

Pyrolysis bio-oil and permanent gas contain abundant chemical thermal energy, which is converted into energy through combined heat and power (CHP) processes to offset energy demands in production. The high temperatures required for graphitization cannot be met by recovered thermal energy, so its energy consumption is set as an electricity supply. Heat generated by CHP is simultaneously used for biomass waste drying, biochar impregnation treatment, and pyrolysis processes. In conservative estimates, excess heat is treated as unrecoverable waste heat. Calorific value data for pyrolysis bio-oil and permanent gas originate from Aspen Plus software. Previous studies employed a triangular distribution model to estimate CHP efficiency for biomass products; this research adopts the most probable values from that model: a 25% electrical efficiency and a 52% thermal efficiency [72].

3.6.2 Life cycle assessment

3.6.2.1 Goal and scope

The LCA of this work was conducted to evaluate the climate change impact and cumulative energy usage of the proposed process according to the bio-based product standard SS-EN 16760:2015 [73]. In this LCA study, the functional unit was set to production of 1 kg of the graphite product. It should be noted that the capital equipment and infrastructure were not considered in the LCA since some prior LCA studies have confirmed their marginal contribution to the overall environmental impact [72]. This process centralizes the pyrolysis of biomass, and the catalytic graphitization, which were designed to convert hardwood to practical graphite material. This work combines a laboratory-scale experiment, theoretical modeling, and literature study to present a thorough analysis of the data to assess a 'theoretical' commercial plant. The process model based on Aspen Plus v11.0 was implemented to determine the energy and mass balance in the pyrolysis, graphitization, and product forming processes.

In this process, electricity and heat were produced as coproducts. The electricity and heat were applied for internal usage. The excess heat was recognized as waste heat for a conservative calculation. Excess electricity was exported to the grid as an alternative to the electricity produced from other sources. The ISO 14040-series standard recommends expanding the system to estimate the life cycle impact of the coproduct [74].

3.6.2.2 Life cycle inventory analysis

Life cycle inventory analysis is the second phase of an LCA study, which defines the compilation and quantification of the processes. In this study, LCI data was collected from literature, experimental studies, and modeling studies.

The feedstock biomass waste used in this study was assumed to be sawdust and other forest residue, which are waste products from the forest industry. The information regarding GHG emissions and other environmental impacts of the biomass waste is not defined in the standard SS-EN 16760:2015 [73]. In this study, the emissions from obtaining the biomass waste and direct/indirect land use change were recognized as 0 according to the Revised Renewable Energy Directive, since the biomass waste is defined as ‘advanced feedstock’ in ANNEX IX [75].

The data collected from LCI analysis (found in Supplement III) was used to perform the life cycle impact assessments. The estimation of biomass transportation distance is described in Supplement III. A minimum transportation distance of 50 km, most likely distance of 100 km, and maximum distance of 150 km were chosen. This model was able to cover the distances reported by previous studies [76-78]. The biomass waste load and fuel consumption of the truck were estimated based on the literature [79]. In this study, the life cycle data of catalysts ($\text{Fe}(\text{NO}_3)_3$) was estimated by integrating the environmental impact from the consumption of ferrite (iron oxide) and nitric acid for certain amount of catalyst production. The remaining LCI data is provided in Supplement III.

3.6.2.3 Life cycle impact assessment

Based on IPCC 100-year global warming potential and cumulative energy demand characteristic factors, the results of the life cycle assessment are presented. Life cycle greenhouse gas emissions are defined as the total greenhouse gas emissions generated throughout the entire process. This study considers graphite as a carbon sink, where carbon from the ecosystem is stored in the form of carbon material. The greenhouse gas emissions considered in this section include: 1) the negative emission effect of graphite materials; 2) CO_2 emissions from external energy consumption throughout the entire process. This study defines the cumulative energy demand (CED) for actual graphite material production as the ratio of cumulative energy (in megajoules) required to produce 1 kilogram of graphite.

4 Development of catalytic graphitization processes

This chapter presents a comprehensive summary of the results obtained from the studies reported in Supplement I. The investigations focus on the influence of carbon precursors on catalytic graphitization behavior and the resulting graphite structure. In particular, differences in graphite structure derived from distinct carbon precursors are examined, with emphasis on interlayer spacing, morphology, and graphite yield. The results provide fundamental insights into how precursor properties influence catalytic graphitization processes. In addition, coproducts formed during graphitization are identified and analyzed, offering important evidence for understanding the graphitization mechanisms associated with biochar-derived and bio-oil-derived carbon. These coproducts also suggest potential co-product streams that may enhance the overall process efficiency and commercialization potential of catalytic graphitization. Overall, this chapter demonstrates a preliminary and feasible pathway for converting biomass-derived carbon precursors into bio-graphite via catalytic graphitization.

4.1 Background and aim

Biomass pyrolysis produces two major carbon-containing products: a solid fraction (biochar) and a liquid fraction (bio-oil), both of which represent potential renewable carbon precursors for bio-graphite production. Biochar is a carbon-rich solid characterized by high fixed-carbon content, low volatile matter, and a partially aromatic structure formed during pyrolysis [50]. These properties make biochar a widely investigated precursor for catalytic

graphitization, and numerous studies have demonstrated its suitability for producing graphitic materials. Consequently, biochar has been regarded as one of the most promising biomass-derived feedstocks for bio-graphite production.

In contrast, bio-oil is a complex liquid mixture composed of oxygenated organic compounds, including phenols, acids, ketones, and sugars [80]. Upon thermal treatment, bio-oil undergoes secondary reactions such as cracking, polymerization, and carbonization, leading to the formation of solid carbon residues [81]. Although bio-oil is typically considered a fuel or chemical feedstock, recent studies have shown that bio-oil can also be transformed into graphitic structures [82]. Utilizing bio-oil as a carbon precursor could enable more comprehensive biomass valorization by converting both solid and liquid pyrolysis products into value-added carbon materials.

Despite these advances, a systematic comparison between biochar and bio-oil as precursors for catalytic graphitization remains limited. In particular, the differences in carbon yield, structural evolution, graphitic crystallinity, and by-product formation under identical processing and catalytic conditions have not been fully elucidated. This lack of comparative understanding hinders precursor selection and limits the development of integrated processes that aim to maximize biomass utilization and process efficiency.

The aim of this section is to systematically investigate and compare biochar and bio-oil as carbon precursors for catalytic graphitization. Specifically, pyrolysis-derived biochar and bio-oil were mixed with iron powder at a mass ratio of 1:1 and subjected to graphitization in a horizontal tube furnace at 1300 °C under an inert nitrogen atmosphere (flow rate: 200 mL min⁻¹). The thermal program consisted of heating from 25 to 600 °C at 5 °C min⁻¹, holding at 600 °C for 1 hour, heating from 600 to 1300 °C at 30 °C min⁻¹, holding at 1300 °C for 3 hours, followed by natural cooling to room temperature. By applying identical catalytic systems and thermal conditions, this study isolates the effect of precursor properties and provides insight into their influence on graphite yield, morphology, crystallinity, structural evolution, and coproduct formation. The results establish a fundamental basis for selecting suitable biomass-derived carbon precursors and for developing feasible and scalable bio-graphite production pathways.

4.2 Results of lab-scale experiments

4.2.1 Characterization of the bio-oil precursor

The chemical composition and functional group distribution of the bio-oil precursor were characterized using FTIR and GC-MS. The GC-MS chromatogram, and identified compound distribution are presented in **Figure 4.1**, and **Table 4.1**, respectively.

GC-MS results (**Figure 4.1**) further revealed the detailed molecular composition of the bio-oil. The bio-oil contains a significantly high abundance of acetic acid, accompanied by other high-concentration compounds such as D-allose, phenols, and guaiacols. The identified compounds, summarized in **Table 4.1**, include phenols and substituted phenolics, furans, ketones, aldehydes, organic acids, and sugar-derived compounds. Phenolic compounds constitute a major fraction of the detected species, originating primarily from lignin decomposition during biomass pyrolysis. Oxygenated aliphatic compounds, such as acids and ketones, were also detected in significant amounts, contributing to the high oxygen content and low thermal stability of the bio-oil.

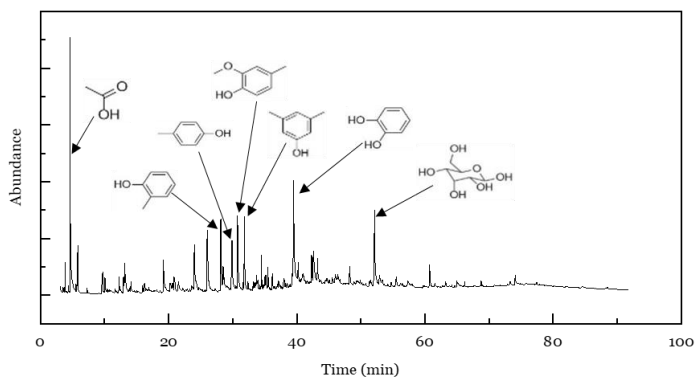


Figure 4.1: GC-MS spectrum of bio-oil sample.

Table 4.1: Classification of chemicals in the bio-oil sample based on GC-MS analysis.

Chemical groups	area %
Guaiacols	11.77
Phenols	31.42
Ketones	7.23
Acids	10.86
Furans	4.31

Sugars	10.01
Benzene and PAHs	1.80
Other oxygenates	0.25
Unknown	22.42

The compound distribution indicates that bio-oil is composed predominantly of low-molecular-weight, oxygen-rich molecules that are thermally unstable and prone to cracking, polymerization, and reforming reactions during heating [83]. These chemical characteristics imply the extensive gas formation and secondary carbonization observed during catalytic graphitization. Unlike biochar, which is already a solid carbonaceous material, bio-oil undergoes substantial chemical transformation prior to forming solid carbon residues, thereby influencing carbon yield and graphitic structural development.

4.2.2 Graphite yield and mass balance

The graphite yield obtained from biochar-derived systems was consistently higher than that from bio-oil-derived one under identical catalytic graphitization conditions. Biochar retained a substantial fraction (74.58%) of its initial carbon mass after graphitization, indicating limited carbon loss during thermal treatment. In contrast, bio-oil-derived bio-graphite exhibited significantly lower solid yields (20.72%), reflecting extensive devolatilization and gas-phase carbon losses during heating.

The lower yield observed for bio-oil-derived carbon was attributed to its liquid-phase origin and high content of oxygenated compounds, which underwent cracking and reforming reactions prior to solid carbon formation. As a result, a larger fraction of carbon was converted into gaseous coproducts rather than retained in the solid graphite product.

4.2.3 Crystallinity and graphitic ordering

XRD patterns of the graphitized samples together with the control sample (biochar without catalyst) are presented in **Figure 4.2**. In the control sample, no sharp diffraction peaks were observed, indicating the absence of graphitic ordering and confirming that thermal treatment alone is insufficient to induce graphitization under the applied conditions. In contrast, both biochar- and bio-oil-derived samples exhibited the characteristic graphitic (002) diffraction peak, demonstrating that catalytic graphitization was successfully achieved in both systems. Nevertheless, noticeable differences in peak shape, intensity, and position were observed between the two precursors.

The bio-oil-derived bio-graphite exhibited a sharper and more intense (002) peak with a reduced full width at half maximum (FWHM), indicating a higher degree of graphitic crystallinity. The (002) peak position shifted closer to 26.55° , corresponding to an interlayer spacing approaching 0.3354 nm , which is characteristic of ideal crystalline graphite [84]. The calculated microcrystalline parameters further confirmed this trend, showing higher degree of graphitization (G%, 71.23%) and larger crystallite sizes along both the c-axis (L_c , 28.78 nm) and a-axis (L_a , 29.90 nm).

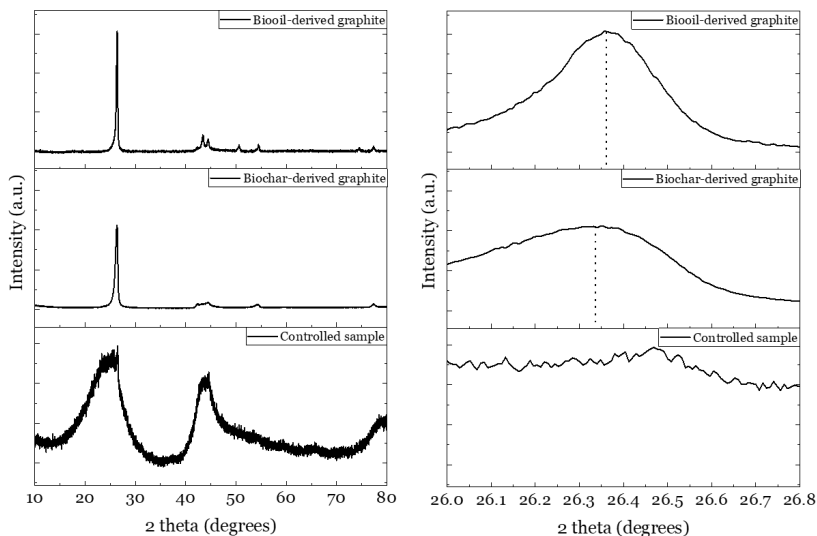


Figure 4.2: XRD spectrum of controlled sample, biochar- and biooil-derived graphite samples.

In comparison, the biochar-derived graphite displayed a relatively broader (002) peak with a smaller peak shift relative to the control sample, indicating less developed graphitic stacking and lower G% (66.54%). The corresponding L_c (18.68 nm) and L_a (20.42 nm) values were also smaller, reflecting limited long-range ordering and the presence of smaller graphitic domains. These results highlight that while both precursors can be successfully graphitized in the presence of a catalyst, bio-oil-derived carbon undergoes more extensive structural reorganization toward well-ordered graphite. These results demonstrate that bio-oil provides a more favorable structural framework for catalytic graphitization, enabling more effective development of stacked graphene layers.

Raman spectra of the graphitized samples are shown in **Figure 4.3**. All samples exhibited the characteristic bands at 1350 cm^{-1} and 1580 cm^{-1} . The peak at about 1360 cm^{-1} , which is referred to the D band, corresponds to the disordered carbon [85, 86]. The peak at around 1589 cm^{-1} , which is termed the G band, is related to the highly ordered graphite [87]. Additionally, the peak at around 2708 cm^{-1} , known as the 2D band, is assignable to the excellent regular structure of the graphite as well [88, 89]. It should be noted that D and G band were clearly observed for all the samples. But the relative intensities of these bands differed significantly between the two precursor systems.

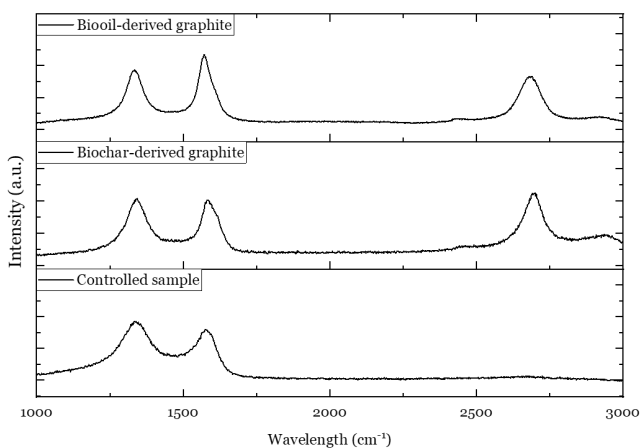


Figure 4.3: Raman spectrum of controlled sample, biochar- and biooil-derived graphite samples.

Both bio-oil- and biochar-derived samples displayed an intense 2D band at approximately 2700 cm^{-1} , whereas this feature was absent in the control sample without catalyst, confirming the successful formation of graphitic structures. Bio-oil-derived graphite exhibited a relatively low I_D/I_G ratio (0.784), indicating a reduced structural disorder and a higher degree of graphitic ordering. In contrast, biochar-derived samples showed higher I_D/I_G ratios (1.004), reflecting a greater concentration of defects and a less complete graphitic reconstruction. These Raman observations are consistent with the XRD results and further demonstrate that bio-oil-derived graphite possesses superior structural ordering compared with biochar-derived graphite under the same graphitization conditions.

4.2.4 Morphology and microstructural evolution

SEM images (**Figure 4.4**) revealed the bio-graphite particles observed from biochar-derived and bio-oil derived samples. A closer view of the particle edge in **Figure 4.4 (a)** reveals a layered structure in bio-oil derived samples. And the layered structure was also found in biochar derived samples in **Figure 4.4 (b)**. The morphology observed in this work exhibits similarities with natural graphite, but is notably thinner [61]. Upon further magnification, bright spots visible in the SEM images (**Figure 4.4 (c)**) are likely residual iron particles from the acid leaching process. The ICP results revealed that 0.033% iron residue remained in graphite samples, attributed to the presence of nano iron particles. Additionally, a small number of spherical graphite particles were observed for the first time in SEM of bio-oil-derived graphite, as shown in **Figure 4.4 (d)**. The fractured spherical graphite reveals a similar layered structure. It is likely that during acid leaching, most spherical graphite particles broke apart, resulting in the formation of numerous irregular particles. TEM analysis provided further insight into microstructural evolution (**Figure 4.5**). Both bio-oil-derived graphite and biochar-derived graphite showed well-aligned, stacked graphene layers with extended lateral dimensions and increased layer continuity.

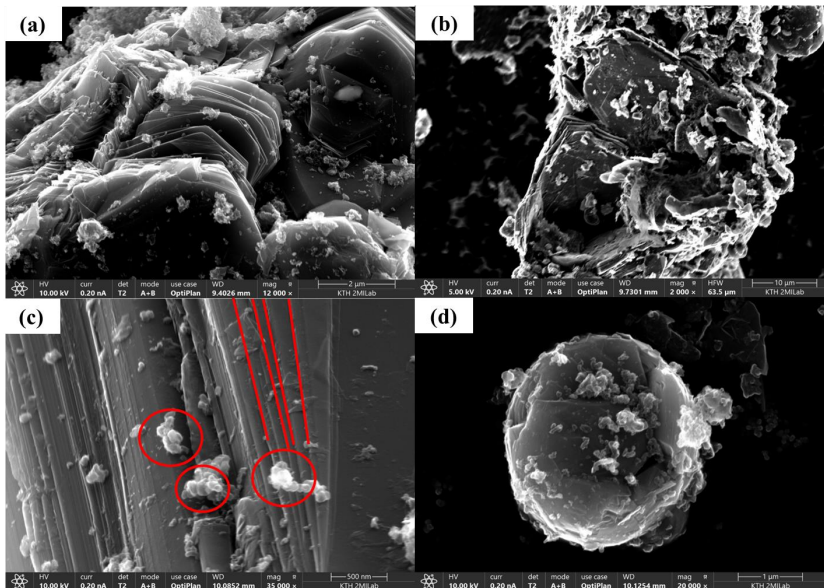


Figure 4.4: SEM images of biochar- and biooil-derived graphite samples.

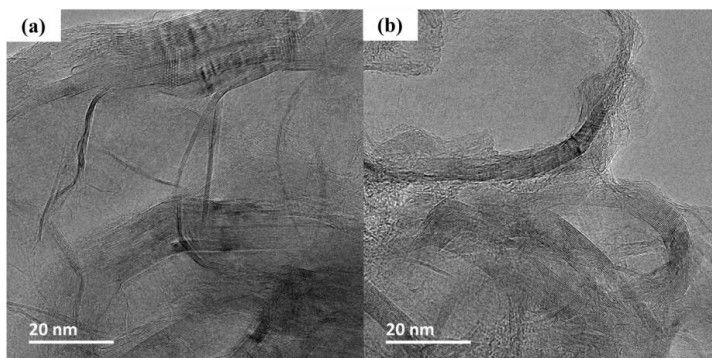


Figure 4.5: TEM images of (a) biochar- and (b) biooil-derived graphite samples.

4.2.5 Gaseous coproducts and graphitization pathways

During catalytic graphitization, Micro-GC was used to monitor gas evolution. As shown in **Figure 4.6**, bio-oil derived systems generated significant amounts of H_2 and CO in the presence of Fe catalysts, which is consistent with catalytic cracking behavior [90, 91], whereas biochar derived systems produced negligible gaseous coproducts, indicating a dominant solid phase graphitization with high carbon retention.

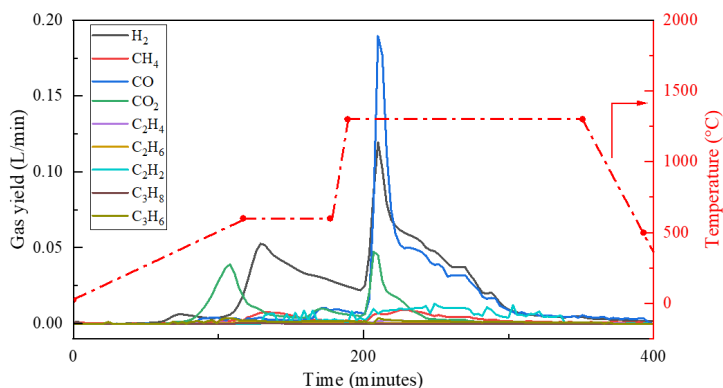


Figure 4.6: The yields of specific gas components during the catalytic graphitization of biooil.

The Micro-GC results reveal fundamentally different graphitization pathways for the two precursors. Biochar undergoes a solid-phase catalytic graphitization, while bio-oil follows a gas-solid coupled reaction route. As shown in **Figure 4.7**, two gas evolution peaks were observed at approximately 600 °C and 1300 °C. The low temperature peak corresponds to catalytic cracking of bio-oil, while the

high temperature peak is associated with an amorphous carbon dissolution and a graphitic reconstruction.

At lower temperatures, complex organic compounds in bio-oil decompose into carbon, H_2 , and CO , with deposited amorphous carbon temporarily deactivating the catalyst sites [92]. At higher temperatures, carbon redissolution restores catalytic activity, promoting graphite formation and increased gas release. During cooling, supersaturation of carbon in the catalyst induces a further graphite precipitation.

This liquid-to-solid formation pathway differs fundamentally from the conventional solid to solid graphitization observed for biochar, where the original carbon framework is largely retained. Instead, bio-oil derived graphitization proceeds via reconstruction of graphite from molecular precursors, explaining the distinct structural features of the resulting bio-graphite.

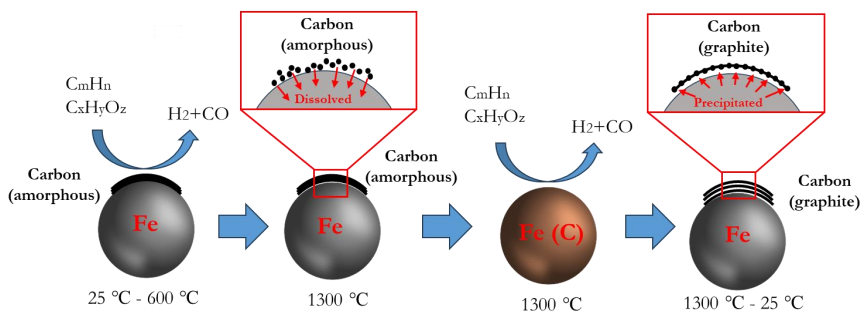


Figure 4.7: Sketch of bio-oil derived bio-graphite formation during catalytic graphitization.

4.3 Summary

Overall, bio-oil-derived bio-graphite exhibited better crystallinity, lower defect density, more favorable morphology, and more developed graphitic microstructures compared with biochar-derived graphite. These results indicate that bio-oil exhibits a greater inherent potential for developing graphitic structures during catalytic graphitization. However, despite its superior graphite quality, the solid yield of bio-oil-derived bio-graphite is significantly low (20.72%) due to substantial volatilization and gas-phase reactions during thermal processing. This low yield represents a fundamental constraint for large-scale production. In contrast, although biochar-derived bio-graphite has relatively lower structural quality, its significantly higher carbon retention rate and stability make it a more practical precursor for scaled-up production. These

findings indicate that precursor selection requires balancing graphite performance with carbon yield, and emphasize that biochar is the preferred precursor for achieving scalable bio-graphite production.

5 Parameter study of catalytic graphitization

This chapter presents a systematic investigation of the key operational parameters affecting the catalytic graphitization of biomass-derived carbon precursors. The results are based on the experimental studies reported in Supplements II and III and focus on the effects of catalyst-precursor mixing strategy, catalyst loading amount, temperature, residence time, and catalyst composition on graphite yield, crystallinity, and microstructural evolution. In addition, the applicability of the resulting bio-graphite is evaluated through its performance as an EAF electrode material and as an anode material in lithium-ion batteries, thereby linking laboratory-scale optimizations with practical applications.

5.1 Background and aim

The results presented in Chapter 4 demonstrate that carbon precursors can influence graphite yield, crystallinity, morphology, and microstructural evolution. While the selection of carbon precursors decisively impacts graphitization outcomes, the efficiency and quality of catalytic graphitization are equally constrained by operational parameters. These parameters affect catalyst activity, carbon migration rates, reaction pathways, and the formation of graphitized microstructures.

Previous studies have demonstrated that factors such as catalyst-precursor mixing strategy, catalyst loading amount, graphitization temperature, residence time, and catalyst composition can significantly affect the degree of graphitic ordering [41, 54, 55]. However, systematic investigations that evaluate these parameters under comparable conditions and link structural evolution to

practical application performance remain limited, particularly for biomass-derived carbon systems.

The aim of this chapter is therefore to systematically investigate the influence of key operational parameters on the catalytic graphitization behavior using biomass-derived carbon precursors. Based on the experimental studies reported in Supplements II and III, this chapter evaluates the effects of catalyst-precursor mixing strategy, catalyst loading amount, graphitization temperature, residence time, and catalyst composition on the graphite yield, crystallinity, and microstructural development. In addition, the practical applicability of the optimized graphite is verified through its performance as an EAF electrode material and as an anode material in LIBs.

5.2 Results of lab-scale experiments

5.2.1 Effect of catalyst compound

To investigate the influence of catalyst compound on catalytic graphitization, Fe powder and $\text{Fe}(\text{NO}_3)_3 \cdot 6\text{H}_2\text{O}$ were compared as catalysts under identical conditions. Both catalysts were applied at a loading of 22.4 wt% Fe relative to the biochar mass, mixed via dry mixing, and graphitized at 1300 °C for 3 hours.

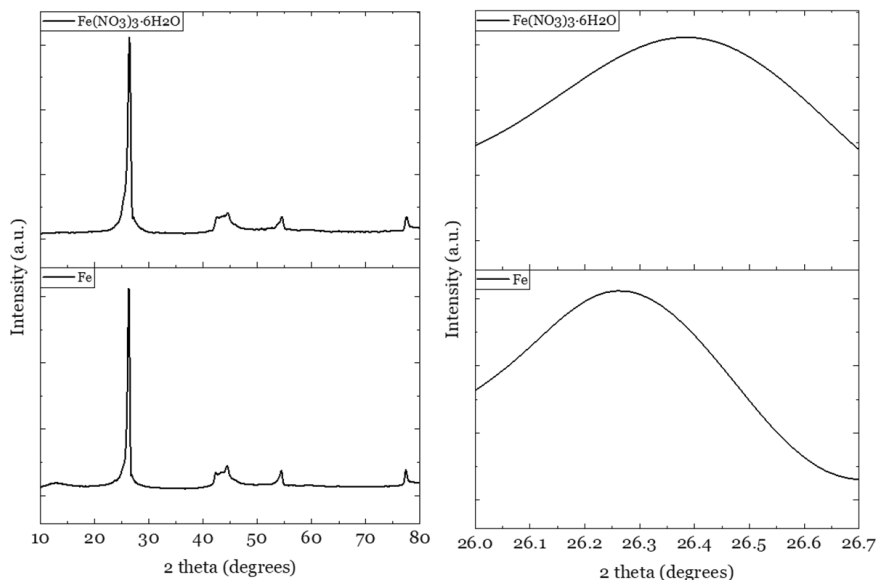


Figure 5.1: XRD spectrum of bio-graphite samples from catalysts of Fe and $\text{Fe}(\text{NO}_3)_3 \cdot 6\text{H}_2\text{O}$.

XRD analysis (**Figure 5.1**) revealed differences in graphitic structural developments between the two catalyst systems. Samples prepared with $\text{Fe}(\text{NO}_3)_3 \cdot 6\text{H}_2\text{O}$ exhibited a (002) diffraction peak that is closer to 26.55° compared with those prepared using iron powder. The calculated d_{002} was closer to the ideal graphite value of 0.3354 nm. Its G% value (88.42%) is much higher than that of bio-graphite sample from Fe powders (62.11%).

In **Figure 5.2**, Raman spectroscopy further confirmed these trends. Although both samples exhibit distinct D, G, and 2D peaks, the $\text{Fe}(\text{NO}_3)_3 \cdot 6\text{H}_2\text{O}$ -catalyzed bio-graphite showed a lower I_D/I_G ratio (0.671), indicating a reduced structural disorder and a higher proportion of ordered sp^2 -bonded carbon compared with the Fe powders-catalyzed sample. These results suggest that metal salts (ferric nitrate hexahydrate) provide a more effective catalytic environment for graphitization than pure metals.

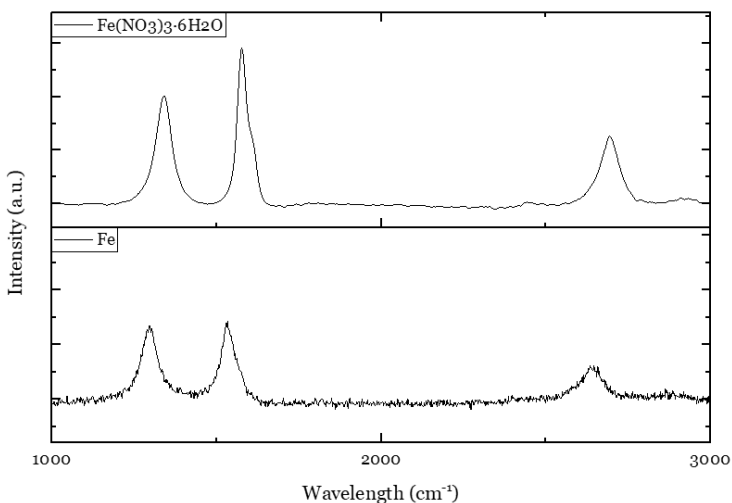


Figure 5.2: Raman spectrum of bio-graphite samples from catalysts of Fe and $\text{Fe}(\text{NO}_3)_3 \cdot 6\text{H}_2\text{O}$.

The better performance of $\text{Fe}(\text{NO}_3)_3 \cdot 6\text{H}_2\text{O}$ can be attributed to its decomposition behavior during heating, which produces finely dispersed iron nanoparticles and promotes intimate contact between catalyst and carbon precursor. In contrast, iron powder tends to agglomerate, limiting catalyst dispersion and reducing effective catalytic surface area. These findings indicate that metal salts are generally more effective than metal powders for catalytic graphitization under the investigated conditions

5.2.2 Effect of catalyst-precursor mixing strategy

The effect of the catalyst-precursor mixing strategy on catalytic graphitization was investigated using $\text{Fe}(\text{NO}_3)_3 \cdot 6\text{H}_2\text{O}$ as the catalyst precursor. A fixed catalyst loading of 22.4 wt% Fe relative to the biochar mass was applied. All samples were graphitized at 1300 °C for 3 h under an inert nitrogen atmosphere to isolate the influence of mixing method. Two mixing strategies, dry mixing and wet impregnation, were compared.

The XRD patterns of the graphitized samples are shown in **Figure 5.3**. Both mixing strategies resulted in graphite structures, confirmed by the presence of the characteristic (002) diffraction peak. The (002) diffraction peaks of both prepared samples were close to 26.55°, indicating high G% values (91.32% and 88.42%, respectively). Furthermore, the peak intensities of both sample groups are highly similar. The calculated crystalline sizes L_c (16.01 nm) and L_a (13.20 nm) for the wet-impregnated samples are comparable to those of the dry-mixed samples (18.54 nm and 12.78 nm).

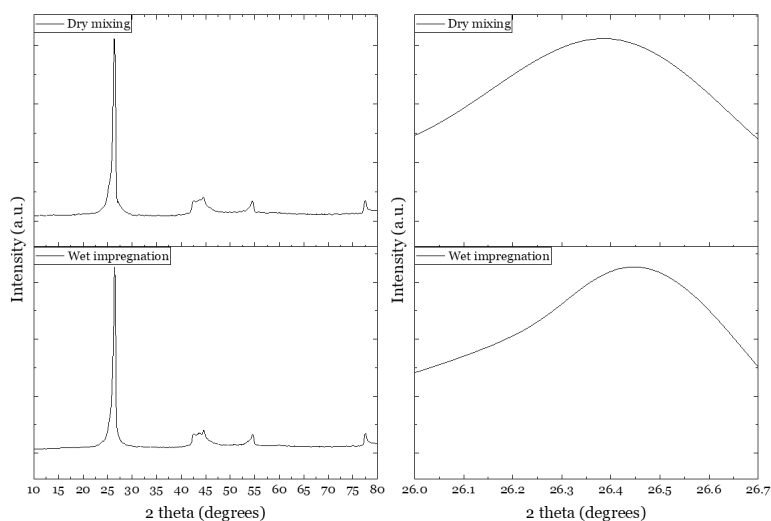


Figure 5.3: XRD spectrum of bio-graphite samples from catalysts of wet impregnation and dry mixing of $\text{Fe}(\text{NO}_3)_3 \cdot 6\text{H}_2\text{O}$.

Raman spectroscopy results (**Figure 5.4**) showed a clear difference between the two mixing strategies. All samples showed well-defined G and 2D bands associated with sp^2 -bonded carbon. However, the wet-impregnated samples exhibited a much lower I_D/I_G ratio (0.276) than the dry-mixed samples (0.671), indicating much fewer defects and a more improved graphitic ordering. These

results suggest that wet impregnation facilitates a more effective catalytic graphitization.

The improved performance observed for wet impregnation is attributed to enhanced catalyst dispersion and a more uniform contact between the catalyst and carbon precursor. More uniformly distributed iron species promote a more homogeneous catalytic activity, facilitating carbon dissolution and subsequent precipitation as ordered graphitic layers. In contrast, dry mixing leads to a less uniform catalyst distribution, resulting in localized graphitization and a less consistent structural development.

Overall, the findings show that catalyst-precursor mixing strategy is a key factor in controlling graphitization efficiency and structural quality. Under the same conditions, wet impregnation provides a more effective approach for achieving higher graphitic crystallinity and more uniform microstructural development compared with dry mixing.

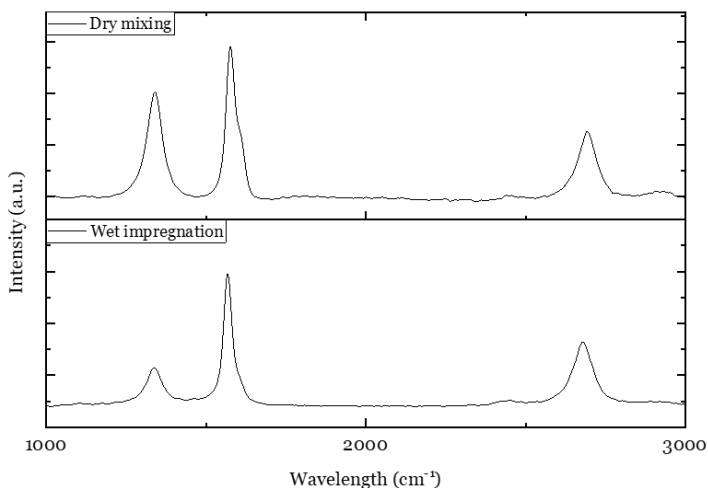


Figure 5.4: Raman spectrum of bio-graphite samples from catalysts of wet impregnation and dry mixing of $\text{Fe}(\text{NO}_3)_3 \cdot 6\text{H}_2\text{O}$.

5.2.3 Effect of graphitization temperature

The influence of graphitization temperature on catalytic graphitization was investigated to illuminate the temperature-dependent structural evolution of biomass-derived biochar. Experiments were conducted at 800, 1100, and 1300 °C with a fixed residence time of 3 hours. $\text{Fe}(\text{NO}_3)_3 \cdot 6\text{H}_2\text{O}$ was used as the catalyst precursor at a loading of 11.2 wt% Fe relative to the biochar mass, and

the catalyst was introduced via wet impregnation to ensure a uniform dispersion. All samples were graphitized under an inert nitrogen atmosphere.

Figure 5.5 shows the XRD patterns of the sample graphitized at different temperatures. At 800 °C, a broad and weak (002) diffraction peak was observed. The peak was located at 26.10°, which was significantly lower than the ideal graphite (002) position at 26.55°, indicating a limited graphitic ordering and a predominantly turbostratic carbon structure. In addition, a sharp peak appearing at approximately 45°, corresponds to the overlap of the (100) and (101) reflections. This suggested the presence of defective or poorly ordered graphitic domains. As the temperature increased to 1100 °C, the (002) peak became more pronounced and shifted toward higher diffraction angles, reflecting a progressive decrease in interlayer spacing and the initiation of graphitic layer stacking. But at 1300 °C, the (002) peak exhibited a significant shift toward the characteristic graphite position, accompanied by a marked reduction in peak width and an increase in peak intensity. Two peaks were more obvious from 40° to 50°. The calculated interlayer spacing (d_{002}) approached the ideal value of crystalline graphite (0.3354 nm), indicating a high degree of structural ordering. Correspondingly, the G% values increased continuously with an increasing temperature (38.43%, 39.10%, and 68.01%), confirming that elevated temperatures promote more complete graphitic structural developments.

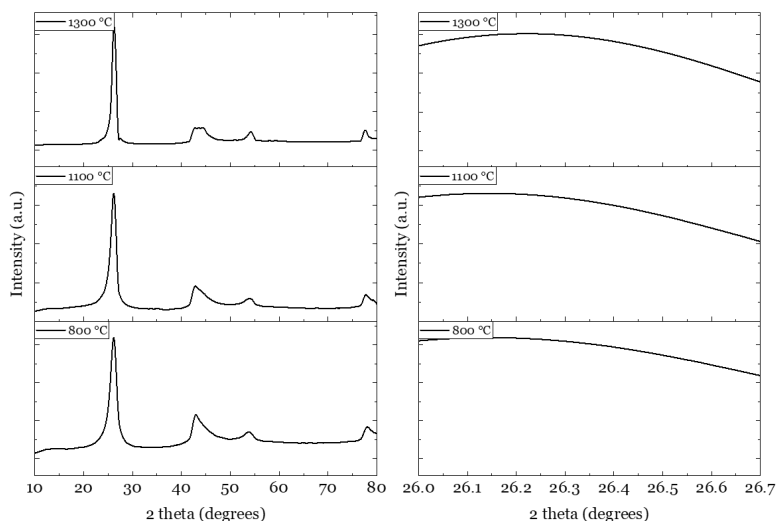


Figure 5.5: XRD spectrum of bio-graphite samples from different temperatures (800 °C, 1100 °C and 1300 °C).

In **Figure 5.6**, Raman spectroscopy results further verified the temperature-dependent evolution of the graphitic structure. All samples exhibited characteristic D and G bands associated with sp^2 -bonded carbon. At both 800 °C and 1100 °C, the relatively high I_D/I_G ratios (0.780 and 0.914) reflected a high degree of structural disorder. As the temperature increased to 1300 °C, the I_D/I_G ratio decreased to 0.342, indicating a partial defect healing and enhanced ordering of the carbon lattice.

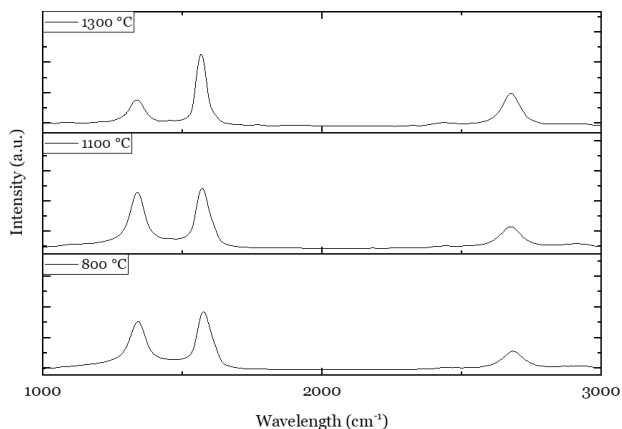


Figure 5.6: Raman spectrum of bio-graphite samples from different temperatures (800 °C, 1100 °C and 1300 °C).

TEM results provided direct evidence of a microstructural evolution with an increasing temperature (**Figure 5.7**). Samples graphitized at 800 °C exhibited short, curved, and poorly aligned graphene layers with limited stacking order, similar to the structure of hard carbon [93]. At 1100 °C, the graphene layers became more extended and partially aligned, with an increased number of stacked layers. At 1300 °C, well-aligned and continuous graphene layers with clear stacking order were observed, confirming the formation of highly developed graphitic microstructures. However, the turbostratic graphitic structure is observed in all the samples.

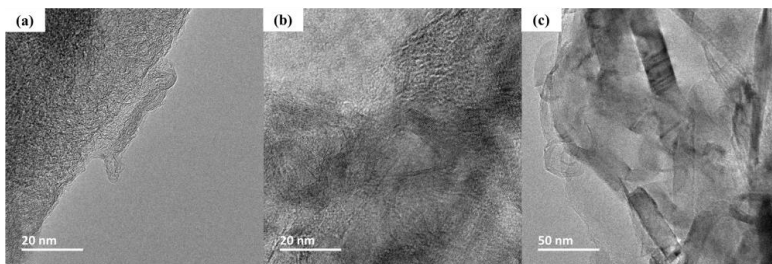


Figure 5.7: TEM images of bio-graphite samples from different temperatures (800 °C, 1100 °C and 1300 °C).

Overall, the results demonstrate a clear temperature-dependent evolution of the carbon structure during catalytic graphitization. Increasing graphitization temperature enhances the carbon atom mobility, promotes catalyst-carbon interactions, and facilitates a structural reorganization toward more ordered graphitic arrangements. As evidenced by XRD, Raman, and TEM analyses, higher temperatures consistently lead to improved graphitic crystallinity, reduced defect density, and more developed graphene layer stacking. These findings indicate that elevated temperatures are favorable for catalytic graphitization and provide a basis for further exploration of higher-temperature graphitization discussed in subsequent chapters

5.2.4 Effect of residence time

The residence time was examined to evaluate its influence on catalytic graphitization and the formation of graphitic microstructures. Experiments were carried out at 1300 °C using $\text{Fe}(\text{NO}_3)_3 \cdot 6\text{H}_2\text{O}$ as the catalyst precursor, with a loading of 11.2 wt% Fe relative to the biochar mass. The catalyst was introduced via wet impregnation, and residence times of 1 hour, 3 hours, and 6 hours were evaluated under an inert nitrogen atmosphere.

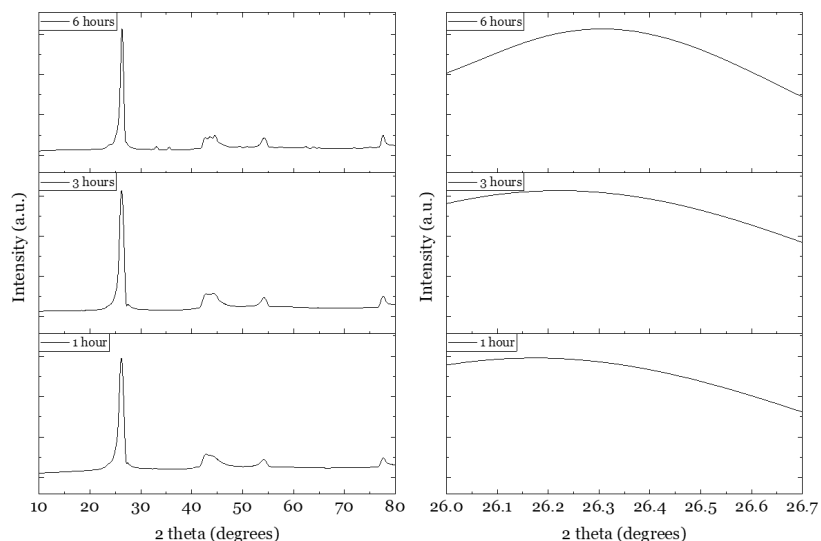


Figure 5.8: XRD spectrum of bio-graphite samples from different residence times (1 hour, 3 hours and 6 hours).

Figure 5.8 presents the XRD spectrums of samples graphitized from different residence times. After 1 hour of treatment, the (002) diffraction peak remained broad and of a low intensity, indicating a limited graphitic ordering and an incomplete layer stacking. Extending the residence time to 3 hours resulted in a clear sharpening and intensification of the (002) peak, together with a shift toward higher diffraction angles. This reflected a reduced interlayer spacing and enhanced graphitic alignment. Increasing the residence time further to 6 hours produced additional changes in peak shape and position.

Raman spectroscopy results (**Figure 5.9**) of the sample treated for 1 hour exhibited a relatively high I_D/I_G ratio, consistent with a high density of structural defects. Increasing the residence time to 3 hours led to a pronounced decrease in the I_D/I_G ratio, indicating a significant defect reduction and improved ordering of the sp^2 carbon network. Prolonging the treatment to 6 hours resulted in only a slight further decrease in the I_D/I_G ratio (from 0.342 to 0.305), confirming that structural ordering has reached a steady stage.

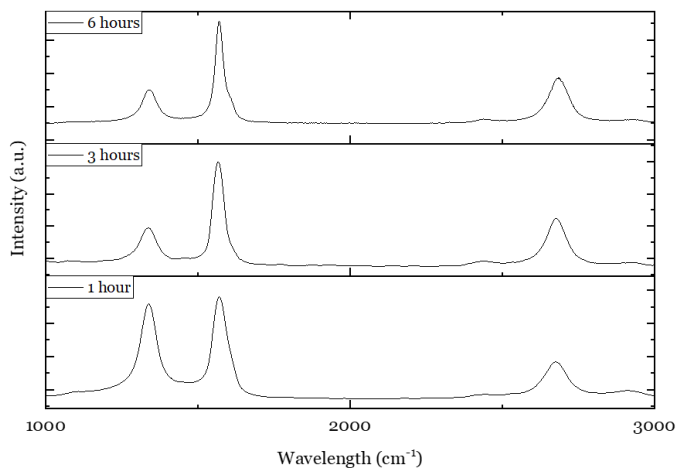


Figure 5.9: Raman spectrum of bio-graphite samples from different residence times (1 hour, 3 hours and 6 hours).

In **Figure 5.10**, TEM images provide direct evidence of microstructural evolution with an increasing residence time. After 1 hour, the carbon structure consisted primarily of short, curved, and poorly aligned graphene layers (**Figure 5.10(a)**). After 3 hours, more extended and better-aligned graphene layers with increased stacking orders were observed, indicating a substantial graphitic development (**Figure 5.10(b)**).

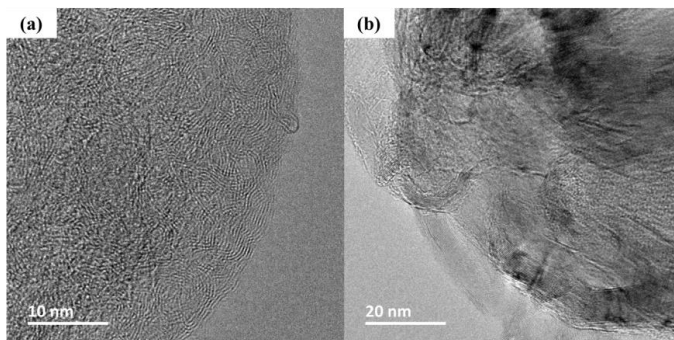


Figure 5.10: TEM images of bio-graphite samples from different residence times (1 hour and 3 hours).

These results indicate that the residence time strongly affects the graphitic structure development during the initial stages of the catalytic graphitization. A treatment duration of 1 hour is insufficient to achieve well-developed graphitic domains under the studied conditions, whereas extending the residence time to 3 hours enables a substantial structural reorganization. This balance between

structural development and residence time is critical for optimizing the energy efficiency and throughput in practical applications.

5.2.5 Effect of catalyst loading amount

The effect of catalyst loading amount on catalytic graphitization was investigated using $\text{Fe}(\text{NO}_3)_3 \cdot 6\text{H}_2\text{O}$ as the catalyst precursor. Catalyst loadings corresponding to 11.2 wt%, 22.4 wt%, and 33.6 wt% Fe relative to the biochar mass were evaluated. The catalyst was introduced to the biochar using a wet impregnation method, which was previously identified as the more effective mixing strategy. All samples were prepared using the same impregnation procedure and graphitized at 1300 °C for 3 hours under an inert nitrogen atmosphere.

In **Figure 5.11**, all samples exhibited the characteristic graphite (002) diffraction peak, confirming successful graphitization at each catalyst loading. Increasing the iron loading amount resulted in a gradual sharpening of the (002) peak and a slight increase in peak intensity. Calculated crystallite sizes L_c showed a steady increase with increasing catalyst loading (11.82 nm, 16.01 nm and 18.56 nm), with the highest values observed at 33.6 wt% Fe. However, the differences in L_a among the three loadings were relatively small (10.20 nm, 13.20 nm and 12.78 nm).

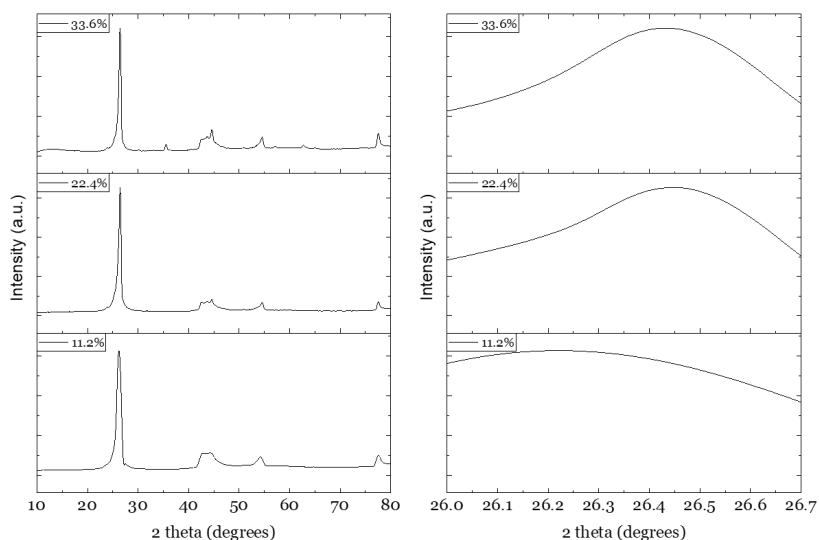


Figure 5.11: XRD spectrum of bio-graphite samples from different catalyst loading amounts (11.2%, 22.4%, and 33.6%).

Raman spectroscopy in **Figure 5.12** further supports these observations. All samples displayed well-defined D and G bands characteristic of graphitic carbon. A slight downward trend in the I_D/I_G ratio was observed with increasing catalyst loading from 11.2% to 33.6% (0.342, 0.275, and 0.208), suggesting a reduction in defect density and improved structural ordering.

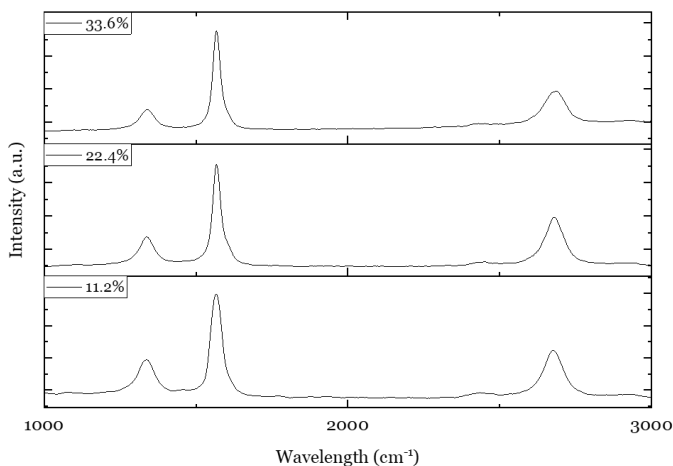


Figure 5.12: Raman spectrum of bio-graphite samples from different catalyst loading amounts (11.2%, 22.4%, and 33.6%).

These results suggest that increasing the catalyst loading amount enhances graphitization by providing additional active sites and improving the carbon dissolution. However, beyond a certain loading amount, further increases in loading resulted in limited improvements in graphite quality. Factors such as the catalyst particle agglomeration and limited carbon accessibility may constrain further structural development at higher loadings. Although 33.6 wt% of Fe produced the highest degree of graphitic ordering under the conditions studied, 22.4% catalyst loadings already achieved comparable graphitization performance, offering potential advantages in terms of material efficiencies and process costs.

5.2.6 Effect of single-, bimetallic-, and trimetallic catalysts

The effect of catalyst composition on catalytic graphitization was systematically investigated using nitrate-based transition metal catalysts, including single-metal, bimetallic, and trimetallic systems. Ferric nitrate hexahydrate ($\text{Fe}(\text{NO}_3)_3 \cdot 6\text{H}_2\text{O}$), nickel nitrate ($\text{Ni}(\text{NO}_3)_2$), and manganese nitrate ($\text{Mn}(\text{NO}_3)_2$) were selected due to their well-documented effectiveness as transition metal

catalysts for graphitization. Catalysts were introduced via wet impregnation with a total metal loading of 22.4 wt% relative to the biochar mass. Graphitization was conducted at 1300 °C for 3 hours under an inert nitrogen atmosphere to enable a direct comparison of the catalytic performances. The catalyst systems evaluated included single-metal catalysts, bimetallic Fe-Ni catalysts with metal ratios of 1:1, 1:2, and 2:1, and a trimetallic Fe-Ni-Mn catalyst with a 1:1:1 ratio.

In **Figure 5.13**, XRD analysis revealed clear differences in graphitic crystallinities among the catalyst systems. Samples produced using hybrid catalysts showed systematically improved graphitic ordering compared with single-metal systems. In particular, the trimetallic catalyst yielded the most significant narrowing and intensification of the (002) diffraction peak, indicating enhanced structural ordering. The corresponding d_{002} approached the ideal value of crystalline graphite (0.3354 nm). The calculated L_c (17.74 nm), L_a (27.96 nm) and G% values (89.29%) were higher than those obtained with single- or bimetallic catalysts. These results indicate that combining multiple transition metals as catalysts enhances the development of long-range graphitic order.

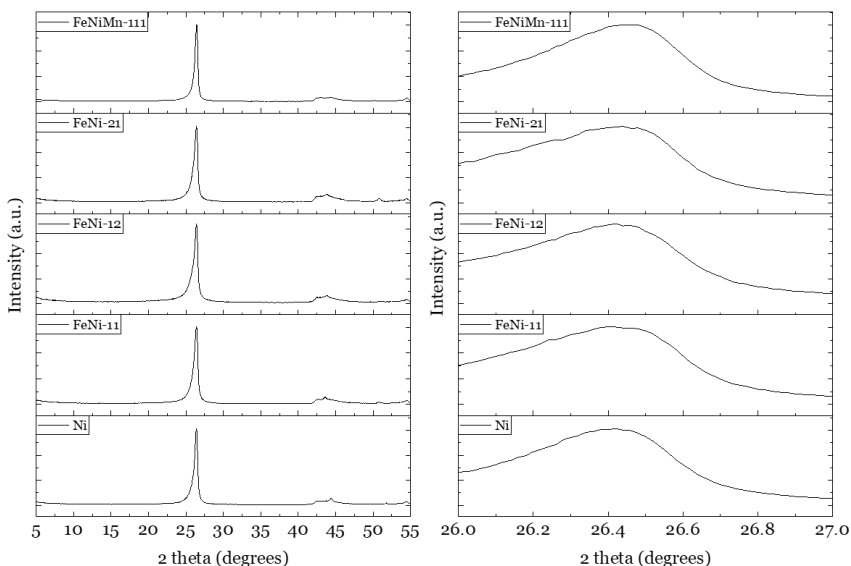


Figure 5.13: XRD spectrum of bio-graphite sample from single, bimetallic and trimetallic catalysts

Raman spectroscopy (**Figure 5.14**) further supported the XRD findings. All graphitized samples displayed characteristic D, G and 2D bands, indicating the

coexistence of ordered and disordered carbon structures. Compared with single-metal catalysts, the hybrid catalyst system exhibited increased G-band intensities and reduced D-band intensities. The bio-graphite produced from bimetallic FeNi-21 and trimetallic catalyst FeNiMn-111 exhibited a low I_D/I_G ratio (0.231 and 0.352), indicating low defect density among the studied systems and an effective reconstruction of sp^2 -bonded carbon networks.

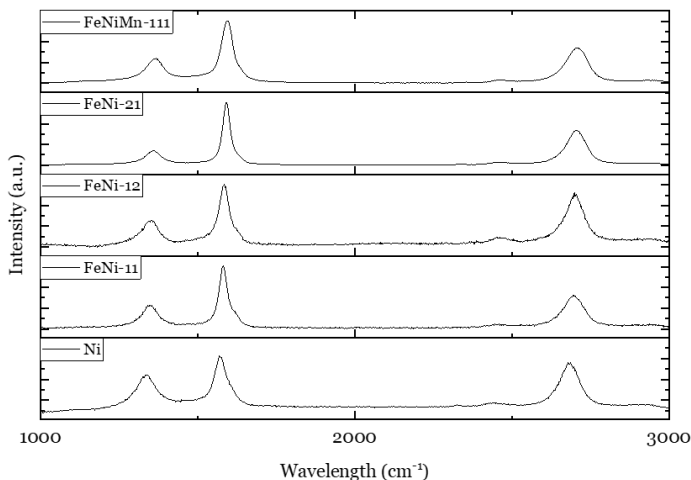


Figure 5.14: Raman spectrum of bio-graphite sample from single, bimetallic and trimetallic catalysts

The crystallinity and microstructural features of the bio-graphite were further examined using TEM. Representative TEM images of the trimetallic catalyst-derived sample are shown in **Figure 5.15(a)**. A typical onion-like microstructure was observed, characterized by concentric catalyst particles encapsulated by multiple overlapping, curved, and well-ordered graphitic shells. The presence of these concentric structures indicates that, during thermal treatment, catalyst particles migrated through amorphous carbon regions, where carbon atoms subsequently dissolved into the metallic phases and precipitated as ordered graphitic layers. This observation is consistent with the widely accepted dissolution-precipitation mechanism of catalytic graphitization reported in the literature [94].

Following acid etching, hollow carbon structures were observed (**Figure 5.15(b)**), confirming that the catalyst particles were largely dissolved and removed from the synthetic bio-graphite matrix. The remaining hollow shells further demonstrate that the metal particles served as active catalytic centers for

graphitic shell growths. A magnified TEM image (**Figure 5.15(c)**) reveals highly ordered graphitic crystallites with clear lattice fringes, where the interlayer spacing was measured to be below 0.34 nm, indicating a well-developed graphite. In addition, the d_{002} calculated from selected area electron diffraction (SAED) patterns matched closely with the values obtained from XRD analysis, further confirming the high crystallinity of the bio-graphite sample.

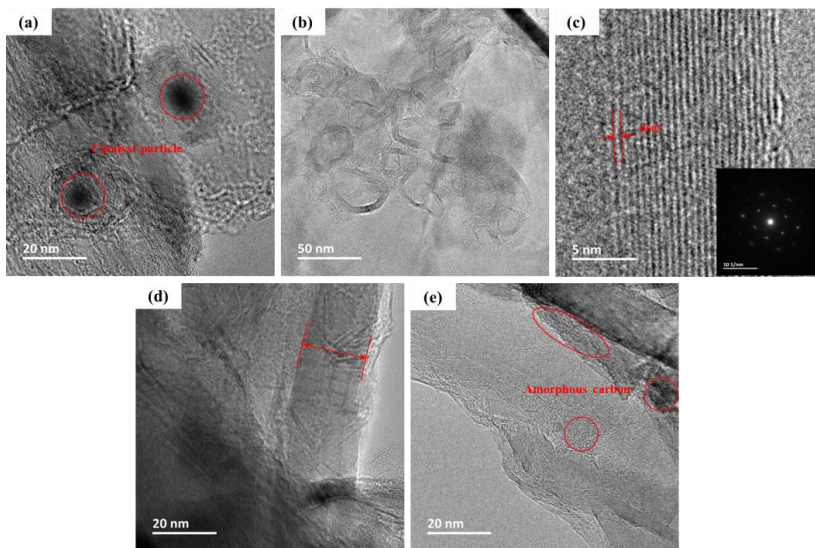


Figure 5.15: TEM images of bio-graphite sample from single, bimetallic and trimetallic catalysts

Extended graphitic domains with long-range stacked carbon layers are shown in **Figure 5.15(d)**, supporting the large crystallite sizes (L_a and L_c) derived from XRD measurements. Nevertheless, localized regions with less ordered, turbostratic carbon and increased interlayer spacing were also observed (**Figure 5.15(e)**). These disordered regions are consistent with the presence of the D band in Raman spectra, indicating that a fraction of amorphous carbon remains even after catalytic graphitization. This suggests that further optimization, such as increasing catalyst loading, increasing temperature or applying additional thermal treatment, may be required to achieve a more complete conversion of disordered carbon into highly ordered graphitic structures.

BET surface area measurements (**Table 5.1**) indicated that all catalyst-treated samples exhibited significantly lower surface areas than the original biochar, reflecting pore collapse and densification during graphitization [95]. However, samples produced using hybrid catalysts generally exhibited higher surface (42-

93 m²/g) areas than those produced (67 m²/g) using single-metal catalysts. This increase is likely attributed to pore formation during acid leaching of alloyed catalyst particles, particularly in trimetallic systems [96]. The higher surface area may negatively affect electrochemical properties [97].

Table 5.1: BET surface areas of original biochar and the bio-graphite samples.

	Biochar	Ni	FeNi-11	FeNi-12	FeNi-21	FeNiMn-111
BET surface area (m ² /g)	324	67	88	69	42	93

The enhanced performance of hybrid catalysts, particularly the trimetallic Fe-Ni-Mn system, can be attributed to synergistic catalytic effects. Alloy formation among Fe, Ni, and Mn increases catalyst stability, carbon solubility, and atomic mobility. In addition, the presence of unpaired d-electrons in these transition metals may facilitate carbon lattice rearrangement, thereby accelerating graphitic structural development [98].

It is important to note that the use of nitrate-based catalysts introduces practical considerations relevant to the process feasibility. During thermal decomposition of metal nitrates, nitrogen oxides (NO_x), primarily NO₂, were released. In the experimental setup, these gases were absorbed in the washing system, where NO₂ dissolved in water and formed nitric acid (HNO₃), as evidenced by the acidic nature of the condensate. This phenomenon represents a potential environmental and operational challenge for large-scale implementation.

The findings indicate that catalyst composition is a critical determinant of catalytic graphitization efficiency. Hybrid catalyst systems exhibit superior performance compared with single-metal catalysts, particularly in enhancing graphitic ordering and microstructural evolution, with the trimetallic Fe-Ni-Mn catalyst demonstrating the highest effectiveness. Nevertheless, the environmental concerns associated with nitrate-based catalysts highlight the importance of integrating catalytic performance with sustainability considerations in the development of scalable bio-graphite production processes.

5.3 Application validation

To demonstrate the practical applicability of the bio-graphite produced via catalytic graphitization, representative samples were evaluated in two technologically relevant applications: consumable electrodes for EAF and anode materials for LIBs. These applications represent the two major industrial applications on usage of graphite and serve as critical benchmarks for assessing their functional performance.

5.3.1 Performance as EAF electrode material

For EAF electrode validation, bio-graphite produced using 22.4 wt% Fe catalyst via wet impregnation and graphitized at 1300 °C for 3 hours was selected, as this condition provided a balanced combination of graphite yield and structural quality. The bio-graphite powder was fabricated into electrode rods using bio-oil as a renewable binder, resulting in a completely bio-based graphite electrode.

In **Table 5.2**, the results of electrical resistivity measurements showed that the fabricated electrodes exhibited a resistivity below 5 $\mu\Omega$ m, which is comparable to commercial graphite electrodes (8.5-9 $\mu\Omega$ m) and meets the conductivity requirements for metallurgical applications. To further demonstrate feasibility, a laboratory-scale EAF prototype was constructed. The operational behavior is documented in videos in supplement III.

Table 5.2: Resistivity properties of graphite electrodes.

	Diameter (m)	Length (m)	Height (m)	Resistance (Ω)	ρ ($\mu\Omega$ m)
Electrode 1	0.02	0.023	-	0.000147	2.01
Electrode 2	0.013	0.016	-	0.000416	3.45

Stable electric arcs were successfully generated when both electrodes were bio-graphite, confirming sufficient electrical and thermal performance. Subsequent metal melting experiments were conducted by replacing one bio-graphite electrode with pure metal samples, including copper, aluminum, and iron. All tested metals were successfully melted under steady arc conditions. Based on the lab-scale melting experiments, the estimated bio-graphite electrode consumption rates were approximately 1.2 kg t⁻¹ for copper, 11 kg t⁻¹ for aluminum, and 49 kg t⁻¹ for steel production (**Table 5.3**). These values are higher than those of conventional EAF graphite electrodes (1.4-2.5 kg t⁻¹ for steel production). But the bio-graphite electrodes still exhibited a promising potential

for metallurgical applications. Detailed experimental procedures and results are provided in Supplement III and its supplementary materials.

Table 5.3: Consumption number of bio-graphite electrodes for melting per ton of metals.

	Cu (kg t⁻¹)	Al (kg t⁻¹)	Steel (kg t⁻¹)
Bio-graphite electrode	1.18	11.01	49.41

5.3.2 Electrochemical performance as LIB anode material

The electrochemical performance of bio-graphite as an anode material for LIBs was evaluated using half-cell configurations. The bio-graphite sample produced using the trimetallic hybrid catalyst (Fe-Ni-Mn, 1:1:1 molar ratio) at 22.4 wt% total metal loading, graphitized at 1300 °C for 3 hours via wet impregnation, was selected based on its superior structural characteristics, as discussed in Section 5.2.

Galvanostatic charge-discharge tests were conducted within a voltage window of 0-3.0 V vs. Li/Li⁺ at a current density of 20 mA g⁻¹ (**Figure 5.16**). The initial discharge curves exhibited a broad plateau around 0.71 V, corresponding to solid electrolyte interphase (SEI) formation, followed by distinct plateaus between 0.21 and 0.084 V associated with Li⁺ intercalation into graphitic layers [99]. The bio-graphite sample delivered an initial discharge capacity of 387.24 mAh g⁻¹ and a reversible charge capacity of 292.57 mAh g⁻¹, corresponding to an initial coulombic efficiency of 75.55%. These features confirm the presence of well-developed graphitic structures. In **Figure 5.17**, differential capacity (dQ/dV) plots further revealed a characteristic staging behavior typically observed in graphite intercalation compounds [100].

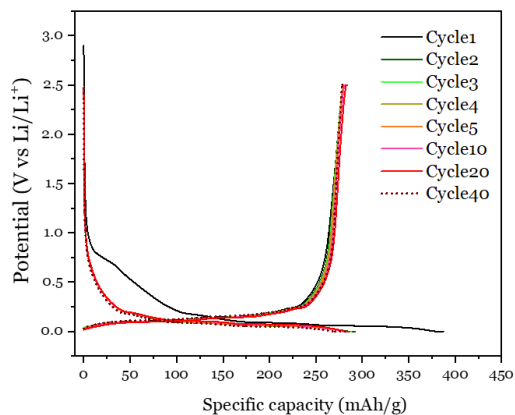


Figure 5.16: Galvanostatic charge-discharge performance of obtained bio-graphite.

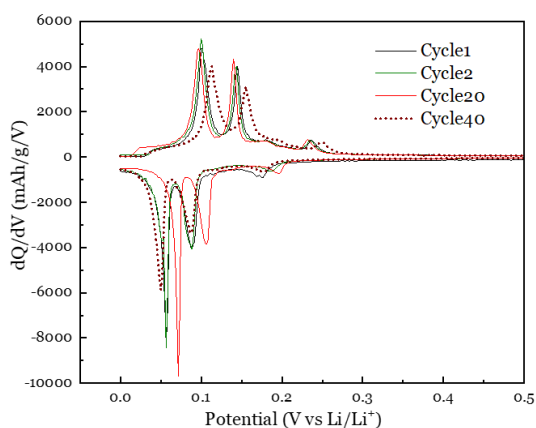


Figure 5.17: Differential capacity (dQ/dV vs Potential) curves at 1st, 2nd, 20th and 40th cycles.

Long-term cycling performance was evaluated over 100 cycles at 20 mA g^{-1} (**Figure 5.18**). The bio-graphite retained a capacity of approximately 279 mAh g^{-1} after 100 cycles, corresponding to a capacity retention of 98.73%. The coulombic efficiency stabilized between 95% and 100% during cycling, indicating an excellent electrochemical stability.

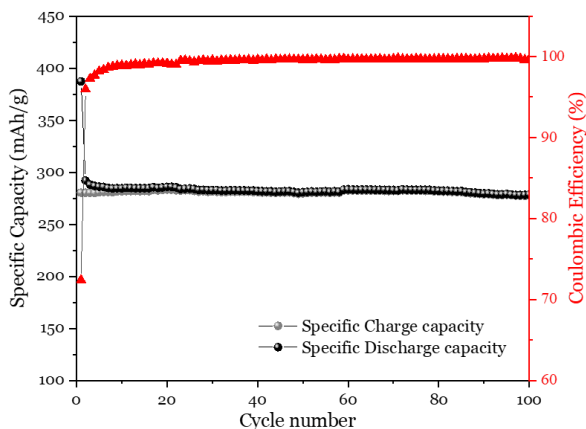


Figure 5.18: Long-term cycling performance (100 cycles) of obtained bio-graphite sample at 20 mA g^{-1} .

Although the electrochemical performance of the bio-graphite approached that of commercial graphite anodes, the reversible capacity and initial coulombic efficiency remained slightly lower. This behavior is attributed to residual amorphous carbon and a relatively high surface area, which promotes an electrolyte decomposition and SEI formation during initial cycling [22]. These findings suggest that further optimization, such as additional heat treatment or surface area reduction, are required to fully match the commercial graphite performance.

5.4 Summary

In this chapter, the catalytic graphitization of biochar was systematically examined with a focus on key operational parameters that affect the bio-graphite formation and quality. The results demonstrate that catalyst compound, mixing strategy, temperature, residence time, catalyst loading amount, and catalyst composition collectively determine the extent of graphitic ordering, crystallite growth, and microstructural evolution. Metal salt catalysts, particularly ferric nitrate hexahydrate, were shown to outperform pure metal powders due to their superior dispersion and catalyst-carbon contact. Wet impregnation consistently enhanced the graphitization efficiency compared with dry mixing by promoting a homogeneous catalyst distribution. Increasing the graphitization temperature and residence time significantly improved the structural ordering. While higher catalyst loadings provided improvements, the effect becomes limited once a certain amount is exceeded. Among catalyst compositions, hybrid systems, especially the trimetallic Fe-Ni-Mn catalyst,

exhibited the strongest synergistic effects, yielding the highest degree of graphitization and most developed microstructures through enhanced dissolution-precipitation behavior. Application validation further confirmed that the bio-graphite meets functional requirements for both EAF electrodes and LIB anodes, demonstrating low electrical resistivity, stable metal melting performance, reasonable reversible capacity, and excellent cycling stability. Overall, this chapter establishes clear structure-process-performance relationships for catalytic graphitization of biomass-derived carbon and provides a solid experimental foundation for process optimization and scale-up discussed in subsequent chapters.

6 Scaling up the process by applying molten pool

6.1 Background and aim

The results presented in Chapters 4 and 5 demonstrate that catalytic graphitization is an effective approach for converting biomass-derived carbon into graphitic materials with good crystallinity and promising application performance. However, these studies also reveal inherent limitations that constrain scalability and industrial implementation. In particular, while wet impregnation of metal salts enables effective catalyst dispersion within carbon precursors, it also leads to a high residual ash content in the final bio-graphite due to the nanoparticles of catalyst residuals. Moreover, the reliance on metal salts-based catalysts results in NO_x emissions during thermal decompositions, which are additional environmental and operational challenges. These limitations highlight the need for alternative process configurations that can deliver high-quality bio-graphite while simplifying the catalyst recovery and reducing the environmental impact.

Therefore, a laboratory-scale experiment was conducted by using pure iron powder as catalysts. Insights gained from the experiment revealed a previously unreported phenomenon: at sufficiently high temperatures, iron catalysts undergo melting and induce a distinct phase separation between graphitized carbon and molten metal. Specifically, due to the different densities, graphitized carbon accumulates above the molten iron phase, while the dense metal phase settles at the bottom of the reactor. This behavior enables partial physical separation of catalyst and graphite without chemical purification. Inspired by these observations, a molten metal pool-based catalytic graphitization strategy

was developed in this work. To the best of the author's knowledge, this process configuration has not been implemented in prior catalytic graphitization studies and represents a novel approach to bio-graphite production.

This chapter includes a two-stage experimental strategy combining laboratory-scale experiments with pilot-scale demonstration, reported in Supplement IV. At the laboratory scale, sawdust-derived biochar is mixed with iron powder at systematically varied metal-to-carbon ratios to evaluate the degree of graphitization and to examine phase behavior under high-temperature conditions. These experiments establish the fundamental feasibility of metal-pool-assisted graphitization and identify key operating windows for scale-up.

Building on the laboratory findings, a pilot-scale study is conducted using an induction furnace to establish a stable molten iron pool. In this configuration, biochar is introduced into the molten metal, and gas injection is employed to enhance mixing and promote flotation of graphitized carbon for a direct collection at a high temperature. This approach enables separations of bio-graphite from molten metal, prevents carbide formation during cooling, and significantly reduces the residual metal content in the final product.

The aim of this chapter is to evaluate molten metal pool-based catalytic graphitization as a scalable and environmentally favorable pathway for bio-graphite production. Through systematic parameter design in laboratory-scale experiments and subsequent validation in pilot-scale trials, this chapter examines the feasibility of pure-metal-catalyzed graphitization and the effectiveness of physical phase separation for catalyst recovery. In addition, the electrochemical performance of the derived bio-graphite is assessed in lithium-ion battery half- and full-cell configurations to verify its long-term stability and application potential. Together, these investigations provide insights into the industrial relevance and practical viability of this novel graphitization process.

6.2 Results of lab-scale experiments

6.2.1 Characterization of graphite

The structural evolution of bio-graphite produced using pure iron powder as catalyst was first evaluated at different iron-to-biochar mass ratios (1:1, 3:1, 5:1, and 10:1). XRD and Raman spectroscopy were employed to assess the degree of graphitization and crystalline ordering after high-temperature treatments at 1600 °C for 1 hour.

In **Figure 6.1**, XRD patterns revealed a clear dependence of graphitic structure development on the iron loading. At lower iron-to-biochar ratios (1:1 and 3:1), the samples exhibited relatively broad and weak (002) diffraction peaks, indicating a limited graphitic ordering and the presence of significant turbostratic or amorphous carbon. Increasing the iron content to a ratio of 5:1 resulted in a noticeable sharpening of the (002) diffraction peak and a slight shift toward higher diffraction angles, suggesting improved layer stackings and reduced interlayer spacings. However, the residual disorder remained evident from the peak position.

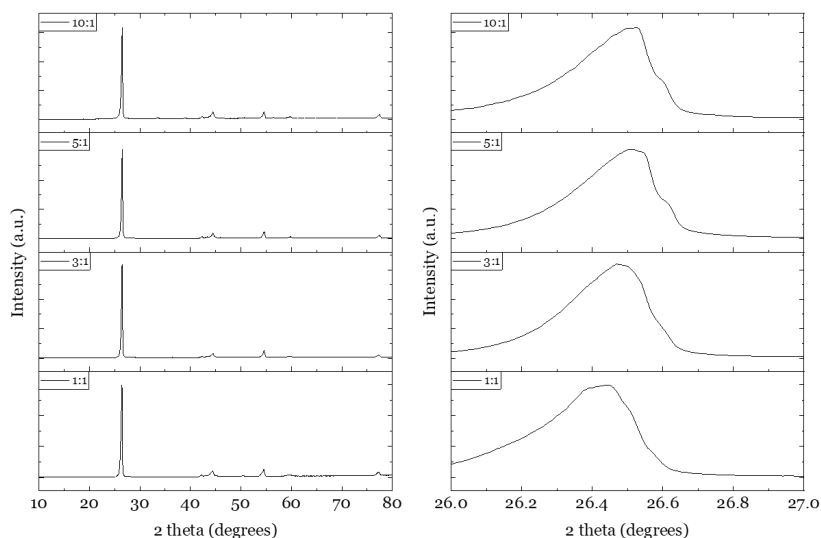


Figure 6.1: XRD spectrum of bio-graphite samples from the ratios of 1:1, 3:1, 5:1 and 10:1.

At the highest iron-to-biochar ratio of 10:1, a well-defined and intense (002) diffraction peak was observed. The calculated d_{002} approached that of ideal graphite, and the crystallite stacking height of L_c (35.0 nm) and lateral size of L_a (39.7 nm) increased markedly. These results indicate that a sufficiently high metal content is required for effective catalytic graphitization when using pure metal powders, in contrast to nitrate-based catalysts where lower metal loadings are typically sufficient.

Raman spectroscopy (**Figure 6.2**) further showed that samples prepared at lower iron loadings displayed relatively high I_D/I_G ratios, reflecting a high degree of structural disorder. The presence of 2D band further confirmed the formation of well-developed graphitic domains at high iron loadings. With an increasing

iron content, the intensity of the G band increased relative to the D band, and the I_D/I_G ratio decreased progressively. The sample prepared at a 10:1 iron-to-biochar ratio exhibited the lowest I_D/I_G ratio (0.05), indicating the highest degree of graphitic ordering among the tested conditions.

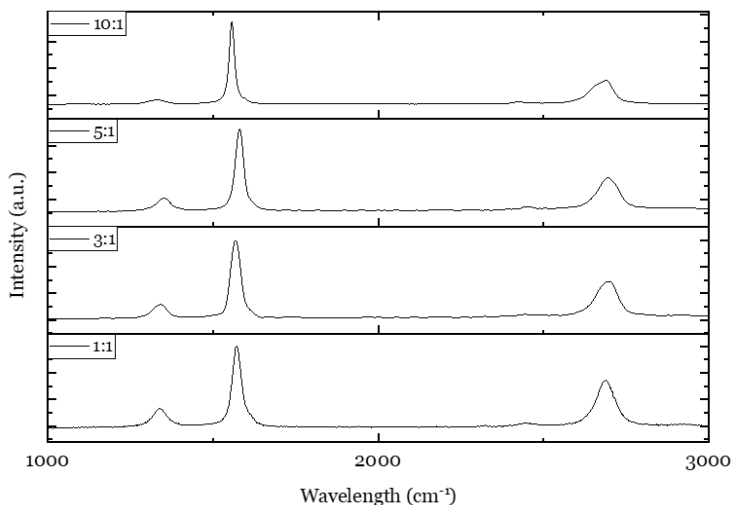


Figure 6.2: Raman spectrum of bio-graphite samples from the ratios of 1:1, 3:1, 5:1 and 10:1.

Overall, these results demonstrate that pure iron powder can effectively catalyze biochar, but only when present in sufficiently large quantities and at higher temperatures. This finding highlights a key distinction between metal powder catalysts and metal salt-derived catalysts and provides critical guidance for process design in molten-metal-based systems.

6.2.2 Physical separation behavior and catalyst redistribution

In addition to enhanced graphitization, a distinct physical separation phenomenon was observed during the high-temperature treatment, particularly at higher iron loadings (**Figure 6.3**). For samples prepared with an iron-to-biochar ratio of 10:1, a clear phase separation occurred after heating and cooling. A dense iron lump was observed at the bottom of the crucible, while the graphitized carbon was recovered predominantly as a powder phase above the metal. This separation was evident and reproducible during multiple experiments.

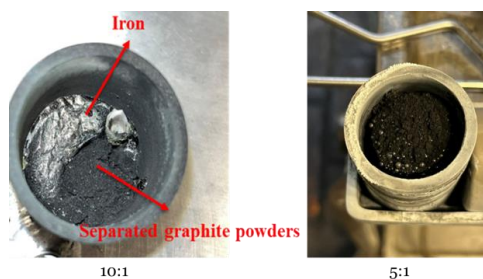


Figure 6.3: Photographs of samples after graphitization (10:1 and 5:1).

In contrast, for samples prepared at a ratio of 5:1, only partial separation was observed. Although some iron agglomerates formed during heating, a substantial fraction of iron particles remained mixed with the carbon powder after cooling, indicating that the metal content was insufficient to form a molten phase capable of complete separation. At lower ratios (1:1 and 3:1), no discernible phase separation occurred, and iron particles remained uniformly distributed within the carbon matrix.

In **Figure 6.4**, O₂-TGA provided quantitative insight into catalyst redistribution after graphitization. Before heating, the mass loss was less than 5% (**Figure 6.4 (a)**), indicating extremely high iron content in the initial mixture. After high temperature treatment and physical separation, the TGA curve exhibited an obvious mass loss, reflecting the substantially reduced iron content in the recovered bio-graphite compared with the original mixture sample before heating, as shown in **Figure 6.4 (b)**. This substantial reduction confirms that a significant portion of the metal catalyst was separated from the carbon product due to density differences and gravitational settling.

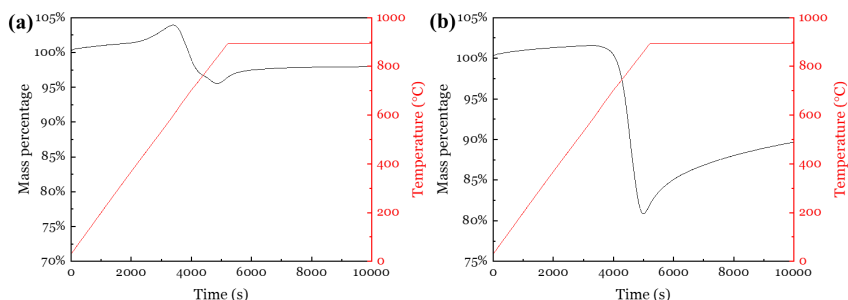


Figure 6.4: TGA curve of the original mixture from the ratio of 10:1 (a) before graphitization, and (b) after graphitization.

SEM and EDS analyses (**Figure 6.5**) further supported these findings. Compared with the original mixture before graphitization, the recovered bio-

graphite powder after heating exhibited a markedly reduced iron signal compared with the pre-heated mixture, and iron was primarily detected as isolated residual particles rather than a continuous phase.

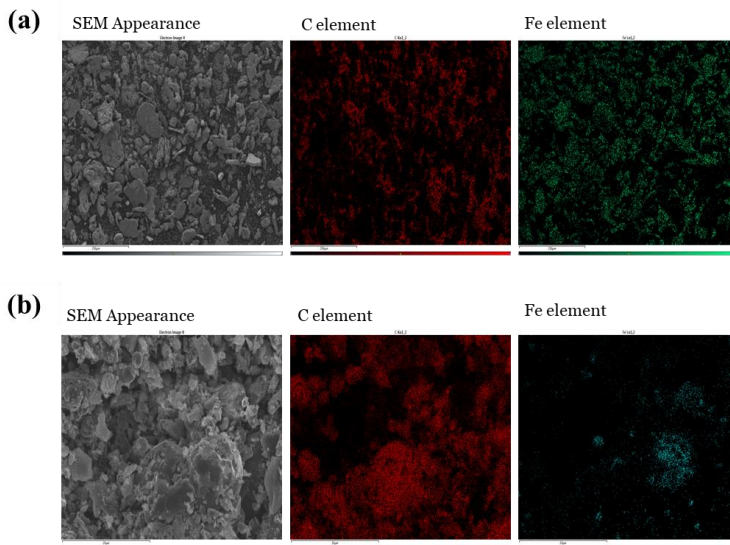


Figure 6.5: SEM and EDS images the bio-graphite from the ratio of 10:1 (a) before graphitization, and (b) after graphitization.

The observed separation behavior of bio-graphite suggests a feasible route for high-temperature extraction. Based on this mechanism, a process concept can be envisioned in which, after a sufficient graphitization duration, inert gas (e.g., argon) is injected from the bottom of the molten metal to promote the flotation and removal of graphite powders from the melt. This finding forms the experimental foundation for the molten metal pool strategy developed in the subsequent sections, where graphite is extracted at high temperature to avoid catalyst residuals in samples.

6.3 Results of pilot-scale experiments

A pilot-scale experiment was conducted to validate molten-metal-pool catalytic graphitization under conditions relevant to semi-continuous production and to demonstrate direct, high-temperature separation of bio-graphite from molten iron without acid purification. The experiments were performed in a 75-kW induction furnace (3 kHz) equipped with a 15-L graphite crucible (capacity 90 kg iron). The furnace was heated to 1600 °C at 50 °C min⁻¹ and maintained for 4 hours under inert protection. During operation, argon was injected through a

bottom lance to generate bubbles, enhancing melt-solid interaction, and promoting flotation and entrainment of graphitized carbon. A glass wool filter was installed at the outlet to capture bio-graphite powders carried with the gas stream. Samples were collected at defined time intervals, initially every 20 min during the first hour and then every 30 min, enabling the evolution of product quality to be tracked as a function of residence time.

6.3.1 Characterization of graphite collected at different reaction times

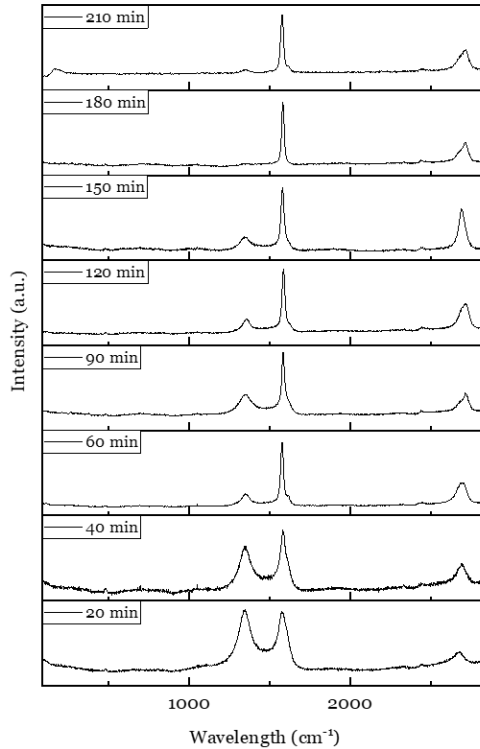


Figure 6.6: Raman spectrum of bio-graphite sample collected at different times.

The time-dependent evolution of graphitic ordering was primarily evaluated by Raman spectroscopy (**Figure 6.6**). The Raman spectra of the collected powders showed a progressive decrease in the D band intensity and a corresponding increase in the G band dominance as the experiment proceeded, indicating a continuous conversion of disordered carbon into ordered graphitic domains. In the early stage (e.g., 20-40 min), the products exhibited strong D bands and relatively high disorder ($I_D/I_G > 1$), suggesting incomplete graphitization. By 60

min, the I_D/I_G ratio decreased below 1, demonstrating a substantial advancement in graphitic ordering within the first hour. With further graphitization, the D band continued to diminish. Samples collected at 120-150 min displayed lower I_D/I_G ratios than earlier samples at 20-90 min, indicating an ongoing structural rearrangement and a defect reduction. Notably, the D band of the bio-graphite powder collected at approximately 180 minutes (and thereafter) nearly disappeared, showing an I_D/I_G ratio approaching zero. The extremely low ratio suggests a near-complete graphitization and the formation of a highly ordered graphite. Taken together, these results indicate that 180 min represents a suitable residence time for continuous operation to ensure a stable production of high-quality bio-graphite.

The high-temperature separation concept was further validated through compositional and impurity analysis. SEM imaging and EDS element mapping of the bio-graphite (210 min) shown in **Figure 6.7** revealed no detection of iron-rich particles in the carbon matrix and no Fe signal in mapping analysis, indicating effective separation of iron during high-temperature extraction. Similarly, in **Figure 6.8**, XPS spectroscopy of combustion residues of bio-graphite revealed no detectable Fe peaks, consistent with the conclusion that iron residues are negligible. Quantitative ICP elemental analysis confirmed that the iron content in recovered graphite is approximately 0.4%, demonstrating that bio-graphite with extremely low catalyst residues can be obtained directly from the molten metal pool without requiring acid leaching processes.

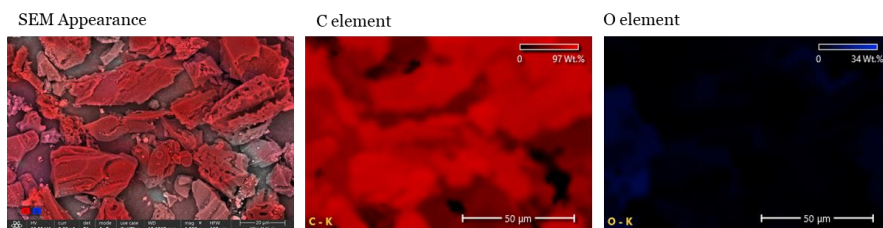


Figure 6.7: SEM and EDS images of bio-graphite sample collected at 210 min.

Together, Raman, SEM-EDS, XPS, and ICP results confirm two essential outcomes of the pilot-scale trial: (i) bio-graphite quality increases with time and reaches a stable, highly ordered state after 180 min, and (ii) direct collection at high temperature enables effective metal-carbon separation, producing bio-graphite with minimal iron contamination.

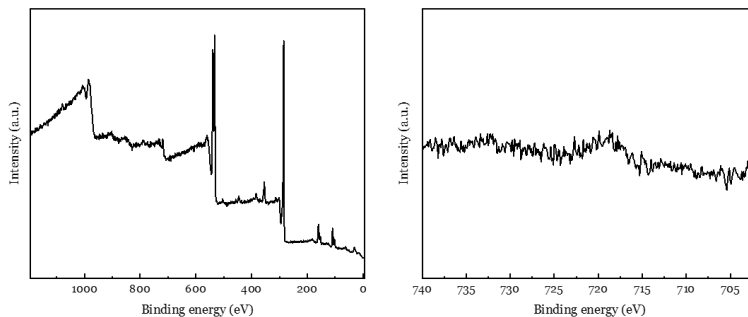


Figure 6.8: XPS full spectra with enlarged range for Fe 2p spectra of the combustion residues of the bio-graphite sample collected at 210 min.

6.3.2 Application of the graphite in half-cell and full-cell Li-ion battery

The pilot-scale graphite production is only meaningful if the resulting material demonstrates strong electrochemical performance in lithium-ion batteries. Therefore, the bio-graphite collected under optimized conditions (the high-quality bio-graphite powder obtained at 180-210 min) was evaluated as an anode material in both half-cell and full-cell configurations.

In lithium half-cells, the bio-graphite exhibited an initial discharge capacity of 392.7 mAh g⁻¹ with an ICE of 72% (**Figure 6.9**). Compared with commercial graphite, the capacity exceeded the typical graphite benchmark (369 mAh g⁻¹ [101]), while the lower ICE was attributed to an increased irreversible capacity associated with SEI formation, which is consistent with the relatively high surface area and porous features of the collected bio-graphite. Long-term cycling results demonstrated excellent stability. After an initial activation period, the reversible capacity stabilized at approximately 520 mAh g⁻¹ with coulombic efficiency around 99%, and the capacity remained above 500 mAh g⁻¹ even after extended cycling (up to 800 cycles).

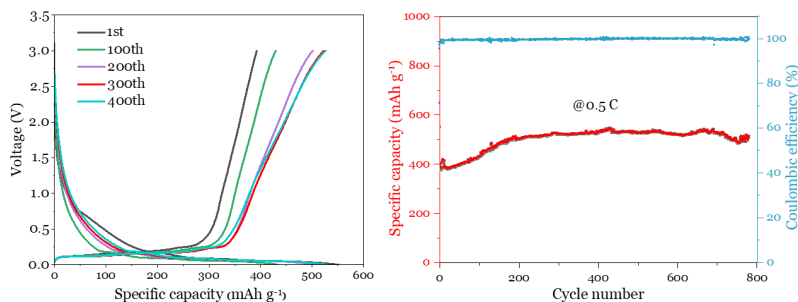


Figure 6.9: Galvanostatic charge-discharge performance and long-term cycling performance (800 cycles) of bio-graphite sample at 0.5 C in half-cell.

The full-cell performance was evaluated using LiFePO_4 (LFP) as the cathode and the bio-graphite as the anode with an N/P ratio of 1.2. **Figure 6.10** shows that the full cell delivered an initial discharge capacity of 141.5 mAh g^{-1} with an ICE value of 88.7%. After 500 cycles at 0.5 C, the cell retained 124.1 mAh g^{-1} , corresponding to approximately 88% capacity retention, while maintaining high coulombic efficiencies of 99-100%. Rate capability tests further indicated that the full cell assembled with the produced bio-graphite delivered higher discharge capacities than a comparable full cell assembled with commercial graphite under the same testing framework, demonstrating the competitiveness of the molten-pool-derived bio-graphite for practical battery applications.

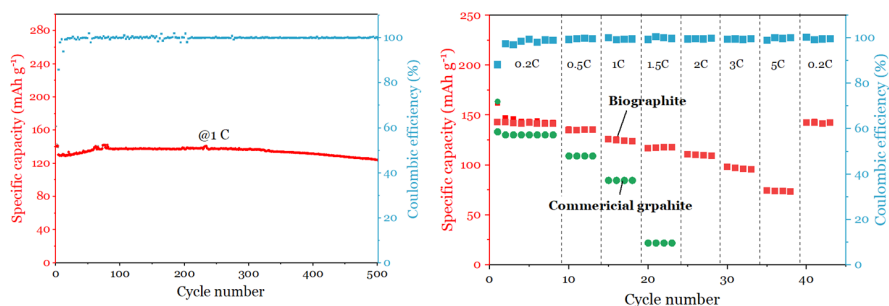


Figure 6.10: Long-term cycling performance (500 cycles) of bio-graphite sample at 1 C and rate capability tests in full cell.

Overall, the electrochemical results confirm that bio-graphite produced and directly separated from a molten metal pool at pilot scale can be used as a high-performance LIB anode material with excellent cycling stability in both half cells and full cells, supporting the industrial relevance of the process developed in this chapter.

6.4 Summary

This chapter demonstrates that molten metal pool-based catalytic graphitization provides a viable and fundamentally different pathway for scaling up the biomass-derived graphite production. Laboratory-scale experiments revealed that pure iron powder can effectively catalyze graphitization at elevated temperatures. However, only at sufficiently high metal-to-carbon ratios, where molten iron formation enables noticeable separation between bio-graphite and metal. The observed flotation of graphitized carbon above the molten iron phase confirmed that density-driven physical separation can substantially reduce catalyst retention in the bio-graphite product. These findings established the mechanistic basis for a high-temperature bio-graphite extraction and motivated the development of a molten metal pool strategy.

Pilot-scale experiments using a 90 kg induction furnace successfully translated this concept into a semi-continuous configuration. Time-dependent characterization showed that graphitic ordering increased steadily with residence time and reached a stable, highly ordered state after approximately 180 minutes, identifying a practical operating window for sustained production. Direct collection of bio-graphite at high temperature enabled effective catalyst separation without acid leaching, yielding products with very low residual iron content, as confirmed by Raman spectroscopy, SEM-EDS, XPS, and ICP analyses. Importantly, the bio-graphite produced at pilot scale exhibited an excellent electrochemical performance in lithium-ion battery half-cell and full-cell configurations. Specifically, it contributed to a high reversible capacity with an outstanding long-term cycling stability.

Overall, the results confirm that molten metal pool-based catalytic graphitization overcomes key scalability and environmental limitations associated with conventional impregnation-based approaches. By integrating efficient graphitization, physical catalyst recovery, and high-temperature product separation, this chapter establishes a robust foundation for an industrially relevant bio-graphite production.

7 Process simulation and life cycle assessment

7.1 Process simulation

Based on the laboratory-scale experimental results, a single integrated process model was developed to evaluate the feasibility of producing bio-graphite powders from biomass waste. The modeled process includes biomass drying and pyrolysis, biochar upgrading and catalytic graphitization, and downstream separation. To maximize the resource efficiency, the energetic coproducts generated during pyrolysis, namely pyrolysis bio-oil and syngas, were transferred to a CHP unit to supply the process with heat and electricity. Excess electricity was assumed to be exported to the grid, while excess heat was conservatively treated as non-recoverable waste heat.

The mass balance of the modeled process (**Figure 7.1**) indicates that approximately 95 kg of bio-graphite powders can be produced per ton of dry biomass. In addition, approximately 327 kg of aqueous-phase bio-oil, 103 kg of organic-phase bio-oil, and 340 kg of permanent gas are co-produced per ton of biomass. Based on their heating values and CHP conversion efficiencies, these co-products can generate approximately 5961 MJ of energy (electricity and heat). In the energy integration strategy adopted here, electricity is assigned to power-intensive units (grinding and graphitization), while recovered heat is assigned to thermal units such as drying and pyrolysis. This configuration highlights a key advantage of utilizing the biomass-based route. Specifically, unlike conventional graphite production, the process requires lower energy and inherently generates internal energy carriers that can substantially offset the external energy requirement.

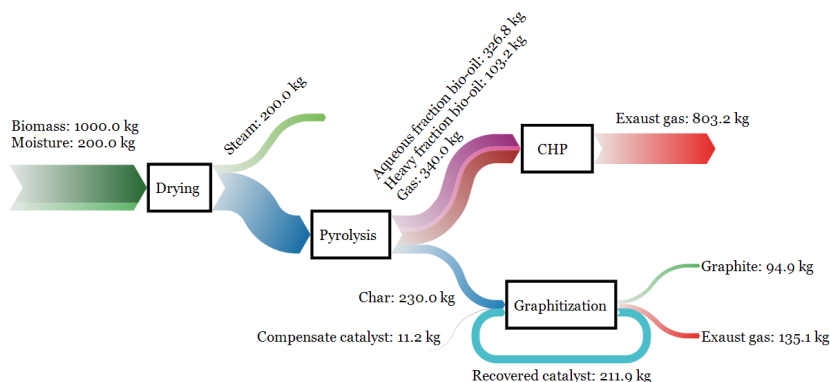


Figure 7.1: The mass flow for process model that produces bio-graphite powders.

7.2 Environmental impact assessment

The primary motivation for using biomass waste as a graphite precursor is to reduce the energy demand and climate impact relative to conventional graphite supply chains. Therefore, the environmental performance of the modeled biomass-to-graphite process was quantified, focusing on CED and GWP. The scope of the process model is presented in **Figure 7.2**, which contains bio-graphite production from industrial biomass waste with internal energy recovery via CHP.

Producing 1 kg of bio-graphite powder requires 34.51 MJ/kg-graphite of cumulative energy input, consisting of 32.71 MJ/kg-graphite from process energy, 1.09 MJ/kg-graphite from chemical production, and 0.71 MJ/kg-graphite from transportation. In parallel, the CHP unit can generate 62.82 MJ/kg-graphite of usable energy, resulting in a net CED of -28.31 MJ/kg-graphite. This negative value indicates that, under the modeled assumptions, the process has the potential to export more energy than it consumes when pyrolysis co-products are fully utilized for energy recovery. In comparison, both conventional graphite supply routes are highly energy intensive. Synthetic graphite production demands an extremely high electricity requirement of 89.9 MJ/kg-synthetic graphite [36]. Natural graphite production, while operating at lower temperatures, still requires a substantial energy input for mining, beneficiation, and chemical purification, leading to a total energy demand of approximately 112.5 MJ/kg-natural graphite [102]. Against this benchmark, the modeled biomass-derived graphite route exhibits a

markedly lower net energy demand, particularly when the energetic co-products are recovered and utilized through a combined heat and power generation.

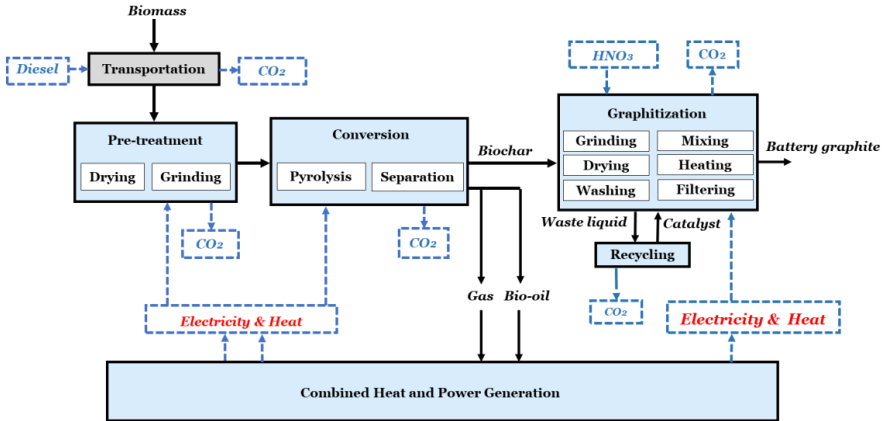


Figure 7.2: Scope of the process model and boundary clarification of the LCA study.

The GWP results show that producing 1 kg of battery graphite emits 1.21 kg CO₂-eq/kg-graphite, including 0.92 kg CO₂-eq/kg-graphite from process operations, 0.07 kg CO₂-eq/kg-graphite from chemical production, and 0.22 kg CO₂-eq/kg-graphite from transportation. When accounting for the exported electricity from CHP, 1.78 kg-graphite CO₂-eq/kg can be offset, yielding a net GWP of -0.57 kg CO₂-eq/kg-graphite. This result suggests that the biomass-based graphite pathway can be net carbon-negative under the modeled system boundary and substitution assumptions. In comparison with conventional graphite production, this represents a strong advantage. Synthetic graphite production is reported to have a particularly high carbon footprint (13.80 CO₂-eq/kg-synthetic graphite) due to its energy intensity, while natural graphite production is driven by mining impacts and purification burdens, emitting 5.32 CO₂-eq/kg-natural graphite [36, 102]. The biomass route achieves substantially lower gross emissions and becomes net negative when the electricity export is accounted for.

Overall, the modeled biomass-waste-to-graphite process is energy efficient and can achieve net-negative climate impact when pyrolysis co-products are recovered and utilized through CHP. Compared with conventional natural and synthetic graphite supply chains, the process demonstrates significantly reduced energy demand and substantially lower GWP, supporting the potential of industrial biomass waste as a sustainable feedstock for graphite production.

8 Conclusions and recommendations for future work

8.1 Overall conclusions

This thesis systematically investigated the production of bio-graphite from renewable carbon sources through catalytic graphitization, progressing from laboratory-scale process development to pilot-scale demonstration and environmental evaluation. The main conclusions are summarized as follows:

Objective 1: Develop catalytic graphitization processes for biomass-derived carbon precursors, including examining renewable carbon feedstocks to establish a feasible method for producing bio-graphite.

Catalytic graphitization was successfully developed for both biochar and bio-oil as renewable carbon precursors. Bio-oil-derived graphite exhibited higher crystallinity ($G\%=71.23\%$) and a lower defect density ($I_D/I_G=0.784$) than biochar-derived graphite (66.54% and 1.004). However, biochar-derived graphite showed a significantly higher carbon yield (74.58%) and process reliability. These findings clarified the distinct graphitization mechanisms and demonstrated that biochar is the more practical precursor to use for a scalable bio-graphite production.

Objective 2: Investigate key operational parameters and catalyst systems to optimize graphitization performance, and validate the application of bio-graphite as an anode material for lithium batteries and as an electrode for EAF applications.

Key operational parameters affecting catalytic graphitization were systematically optimized. Catalyst compound, mixing strategy, temperature, residence time, the loading amount, and catalyst composition were shown to strongly influence graphite crystallinity and microstructure. Hybrid catalysts, particularly trimetallic systems, provided superior graphitic ordering (the highest G% value of 89.29% and the lowest I_D/I_G ratio of 0.231). The optimized bio-graphite demonstrated low electrical resistivities (2.01-3.45 $\mu\Omega$ m) in electric arc furnace electrodes and good cycling performances (279 mAh g⁻¹ at 20 mA g⁻¹ in half cell) as lithium-ion battery anodes.

Objective 3: Develop scalable production strategies as an industrially viable approach and demonstrate the process by conducting pilot-scale experiments.

A novel molten metal pool-based graphitization process was developed based on insights from laboratory-scale experiments using pure metal catalysts. This previously unreported process enabled a physical separation of graphite from molten iron, a reduced residual metal content, eliminated nitrate-derived emissions, and enabled a semi-continuous graphite production. Pilot-scale experiments confirmed the feasibility of producing high-quality graphite with minimal iron contamination and excellent battery performance (124.1 mAh g⁻¹ at 1C in the full cell).

Objective 4: Assess the environmental performance of the proposed process and benchmark biomass-derived graphite against conventional fossil-based graphite production routes.

The energy and environmental performance of the proposed bio-graphite production routes were evaluated using process simulations and life cycle assessments. The results demonstrated a substantially lower cumulative energy demand (34.51 MJ/kg-graphite) and greenhouse gas emissions (1.21 kg CO₂-eq/kg-graphite) compared with conventional fossil-based synthetic graphite (89.9 MJ/kg-synthetic graphite and 13.8 kg CO₂-eq/kg-synthetic graphite) and natural graphite production (112.5 MJ/kg-natural graphite and 5.32 kg CO₂-eq/kg-natural graphite), especially when the coproduct energy recovery was considered (-28.31 MJ/kg-graphite).

Overall, this thesis establishes catalytic graphitization of biochar as a technically viable, scalable, and environmentally favorable pathway for achieving a sustainable graphite production, with demonstrated applicability in both energy storage and metallurgical industries.

A detailed summary of the objectives and results for each supplement is provided in **Table 8.1**.

Table 8.1: Overview of the objectives of the supplements presented in this doctoral thesis with main results.

Supplement	Objectives	Results
I	Investigate the potential of pyrolysis bio-oil as a carbon precursor for catalytic graphitization and compare it with biochar	Bio-oil enables superior graphitic ordering through a gas-solid mediated reconstruction mechanism, while biochar provides a significantly higher solid carbon yield, making it more suitable for a scalable production.
II	Develop a novel trimetallic catalyst for catalytic graphitization to improve the graphitic crystallinity and LIBs electrochemical performance	Compared to single or bimetallic systems, trimetallic Fe-Ni-Mn catalysts exhibit synergistic effects that significantly improve the crystallinity and microstructural developments, leading to enhanced electrochemical performances in LIBs.
III	Identify the key operational parameters for catalytic graphitization, demonstrate the applicability of bio-graphite for LIBs anodes and electrodes, and evaluate environmental performance	Optimized parameters (elevated temperature, increased catalyst loading, and longer residence time) significantly enhance graphitization. Bio-graphite showed stable cycling in LIBs and effective melting in EAFs. LCA confirmed substantially lower energy demand and emissions than conventional graphite.
IV	Optimize the catalytic graphitization process, improve the graphite quality, and develop a new process to enable a semi-continuous production with reduced acid consumption	Developed an unreported process that enables direct high-temperature separation of graphite from the catalyst via a density-driven phase separation, yielding highly ordered graphite with minimal residual metal. The obtained bio-graphite exhibited a high capacity and an ICE in both LIBs half-cells and full-cells.

8.2 Recommendations for future work

Although this thesis has made significant progress in sustainable bio-graphite production, several research directions warrant further exploration to achieve a comprehensive industrial deployment and performance optimization.

First, precursor engineering and pretreatment strategies should be further investigated. Customizing biochar characteristics by controlling pyrolysis conditions, decalcification, or adjusting particle morphologies can reduce structural heterogeneity and enhance catalytic graphitization efficiency. Similarly, upgrading bio-oil or implementing mixed bio-oil/biochar feed systems can balance yield and crystallinity.

Second, a deeper understanding of hybrid catalyst behavior is required. In-situ/operando techniques such as high-temperature X-ray diffraction, in-situ transmission electron microscopy, or synchrotron spectroscopy can directly reveal the alloy formation, carbide evolution, and graphitization nucleation kinetics during the catalytic graphitization. Such insights will support rational catalyst design rather than an empirical optimization.

Third, the molten metal bath process requires advancement toward creating a continuous operation. Future work should focus on reactor design optimization, gas-assisted graphite extraction strategies, and hydrodynamic control to ensure stable graphite recovery while minimizing metal loss. Concurrently, a systematic evaluation is needed of how the molten metal composition, impurity elements, and long-term catalyst stability impact the process.

Fourth, advanced electrode engineering techniques are required to fully leverage bio-graphite in lithium-ion batteries. By reducing surface area, optimizing particle morphology, and applying surface coatings, initial coulombic efficiency and rate performance can be enhanced, bringing performance closer to commercial graphite benchmarks.

Finally, a comprehensive techno-economic analysis incorporating extended life cycle assessments is recommended. Such studies must account for capital costs, catalyst recovery, regional biomass resource availability, and integration with existing metallurgical or bioenergy infrastructure to assess the commercial competitiveness and deployment scenarios.

In summary, this thesis establishes a foundational platform for future research and industrial innovation. Sustained interdisciplinary collaboration across materials science, process engineering, and sustainability analysis is essential to

advance bio-graphite from a promising laboratory material to a cornerstone of sustainable graphite supply chains.

References

1. Burchell, T.D. and T.R. Pavlov, *Graphite: properties and characteristics*, in *Comprehensive Nuclear Materials: Second Edition*. 2020, Elsevier. p. 355-381.
2. Zhao, L., et al., *Revisiting the roles of natural graphite in ongoing lithium - ion batteries*. *Advanced Materials*, 2022. **34**(18): p. 2106704.
3. Olson, D.W., et al., *Natural graphite demand and supply— Implications for electric vehicle battery requirements*. 2016.
4. Pillot, C. *The rechargeable battery market and main trends 2018– 2030*. in *36th annual international battery seminar & exhibit. avicenne energy*. 2019.
5. Echterhof, T., *Review on the use of alternative carbon sources in EAF steelmaking*. *Metals*, 2021. **11**(2): p. 222.
6. Team, G.S.W.E. *From reliance to resilience: Securing Europe’s green graphite supply*. May 12, 2025; Available from: <https://greensteelworld.com/from-reliance-to-resilience-securing-europes-green-graphite-supply>.
7. world, M.r., *Graphite Electrodes Market Size, Share, Growth, and Industry Analysis*. 29 Dec, 2025.
8. Koese, M., et al., *Self-sufficiency of the European Union in critical raw materials for E-mobility*. *Resources, Conservation and Recycling*, 2025. **212**: p. 108009.
9. Zhang, Q.Q., X.Z. Gong, and X.C. Meng. *Environment impact analysis of natural graphite anode material production*. in *Materials Science Forum*. 2018. Trans Tech Publ.
10. Pandey, R., et al., *Energy, greenhouse gas, and water life cycle analysis of synthetic graphite anode production in the United States*. *Environmental Science: Advances*, 2025. **4**(12): p. 2055-2068.

11. Peng, X., et al., *High value utilization of biomass: Moving towards a carbon neutrality future*. Renewable and Sustainable Energy Reviews, 2026. **226**: p. 116477.
12. Gupta, V.K., et al., *Biobased biorefineries: Sustainable bioprocesses and bioproducts from biomass/bioresources special issue*. 2022, Elsevier. p. 112683.
13. Saleh, T.A., *A review on the technologies for converting biomass into carbon-based materials: sustainability and economy*. Bioresource Technology Reports, 2024. **25**: p. 101771.
14. Ike, S. and R. Vander Wal, *Effect of carbonization methods on graphitization of soft and hard carbons*. Carbon Trends, 2024. **16**: p. 100382.
15. Ōya, A. and S. Ōtani, *Catalytic graphitization of carbons by various metals*. Carbon, 1979. **17**(2): p. 131-137.
16. Destyorini, F., et al., *Temperature driven structural transition in the nickel-based catalytic graphitization of coconut coir*. Diamond and Related Materials, 2021. **117**: p. 108443.
17. Yokokawa, C., K. Hosokawa, and Y. Takegami, *Low temperature catalytic graphitization of hard carbon*. Carbon, 1966. **4**(4): p. 459-465.
18. Chehreh Chelgani, S., et al., *A review of graphite beneficiation techniques*. Mineral Processing and Extractive Metallurgy Review, 2016. **37**(1): p. 58-68.
19. Lu, H., et al., *Graphite and its main applications*, in *Functional Carbon Materials*. 2022, IOP Publishing Bristol, UK. p. 6-1-6-28.
20. Zhao, W., et al., *Progress, challenge and perspective of graphite-based anode materials for lithium batteries: A review*. Journal of Energy Storage, 2024. **81**: p. 110409.
21. *Graphite Growth Markets*. Available from: <https://www.northerngraphite.com/graphite-markets/>.
22. Lower, L., et al., *Catalytic graphitization of biocarbon for lithium - ion anodes: a minireview*. ChemSusChem, 2023. **16**(24): p. e202300729.
23. *Graphite, Outlook for key energy transition minerals*. 17 May, 2024, International Energy Agency.
24. *Graphite Electrode Market Innovations 2025-2030 Forecast*. 12 Nov, 2025; Available from: <https://www.openpr.com/news/4311780/graphite-electrode-market-innovations-2025-2030-forecast-el-6>.
25. Bhattacharyya, S., et al., *Graphite: the new critical mineral*. Nature Reviews Materials, 2025: p. 1-14.

26. Quan, Y., et al., *Highly efficient purification of natural coaly graphite via an electrochemical method*. Separation and Purification Technology, 2022. **281**: p. 119931.
27. Weber, L., *On the security of graphite supply*. Mineralogy and Petrology, 2023. **117**(2): p. 387-399.
28. Hwang, J.U., et al., *Properties of synthetic graphite from boric acid-added pitch: Performance as anode in lithium-ion batteries*. SN Applied Sciences, 2021. **3**(6): p. 600.
29. Kulkarni, S., et al., *Prospective life cycle assessment of synthetic graphite manufactured via electrochemical graphitization*. ACS Sustainable Chemistry & Engineering, 2022. **10**(41): p. 13607-13618.
30. Robinson Jr, G.R., J.M. Hammarstrom, and D.W. Olson, *Graphite*. 2017, US Geological Survey.
31. Zondlo, J.W., *Graphite: structure, properties, and applications*. Graphite, Graphene, and Their Polymer Nanocomposites, 2012: p. 1-56.
32. Okada, M., et al., *Review on the high-temperature resistance of graphite in inert atmospheres*. Carbon, 2017. **116**: p. 737-743.
33. Park, J., et al., *Overview of graphite supply chain and its challenges*. Geosciences Journal, 2025. **29**(3): p. 329-341.
34. Yadav, R., A.K. Sharma, and S. Sharma, *Advance Development in Natural Graphite Material and Its Applications: A Review*. Mining, Metallurgy & Exploration, 2025. **42**(1): p. 361-385.
35. *Global New Supply of Environmentally Sustainable Battery Graphite for the Lithium-ion Battery and Smart Technologies Markets*. 17 Apr, 2019, Kibaran Resources Limited.
36. Surovtseva, D., et al., *Toward a life cycle inventory for graphite production*. Journal of Industrial Ecology, 2022. **26**(3): p. 964-979.
37. Genovesi, S., *Graphite for lithium-ion batteries: mineral analysis and global Material Flow Analysis*. 2022.
38. Moradi, B. and G.G. Botte, *Recycling of graphite anodes for the next generation of lithium ion batteries*. Journal of Applied Electrochemistry, 2016. **46**(2): p. 123-148.
39. Hunter, R., J. Ramírez-Rico, and Z. Schnepf, *Iron-catalyzed graphitization for the synthesis of nanostructured graphitic carbons*. Journal of Materials Chemistry A, 2022. **10**(9): p. 4489-4516.
40. Khoshk Rish, S., et al., *Formation mechanism of nano graphitic structures during microwave catalytic graphitization of activated carbon*. Diamond and Related Materials, 2021. **120**: p. 108699.
41. Pourabdollah, K., et al., *Experimental investigation of process parameters during graphitization of catalytic coke*. International Journal of Coal Science & Technology, 2019. **6**(4): p. 611-620.

42. Gai, L., et al., *Evolution of biomass to porous graphite carbon by catalytic graphitization*. Journal of Environmental Chemical Engineering, 2021. **9**(6): p. 106678.
43. Obrovac, M.N., et al., *Reversible lithium insertion in catalytically graphitized sugar carbon*. Electrochemistry Communications, 2015. **60**: p. 221-224.
44. Renda, C., et al., *Influence of the mixing process on the graphitization of phenolic resins*. Ceramics International, 2019. **45**(9): p. 12196-12204.
45. Jabarullah, N.H., A.S. Kamal, and R. Othman, *A modification of palm waste lignocellulosic materials into biographite using iron and nickel catalyst*. Processes, 2021. **9**(6): p. 1079.
46. Hunter, R.D., et al., *The effect of precursor structure on porous carbons produced by iron-catalyzed graphitization of biomass*. Materials Advances, 2020. **1**(9): p. 3281-3291.
47. Zhang, X., et al., *Carbon-based nanomaterials from biopolymer lignin via catalytic thermal treatment at 700 to 1000° C*. Polymers, 2018. **10**(2): p. 183.
48. Zhu, Y., et al., *Hydrothermal carbons/ferrihydrite heterogeneous Fenton catalysts with low H₂O₂ consumption and the effect of graphitization degrees*. Chemosphere, 2022. **287**: p. 131933.
49. Demir, M., et al., *Graphitic biocarbon from metal-catalyzed hydrothermal carbonization of lignin*. Industrial & Engineering Chemistry Research, 2015. **54**(43): p. 10731-10739.
50. Panwar, N., A. Pawar, and B. Salvi, *Comprehensive review on production and utilization of biochar*. SN Applied Sciences, 2019. **1**(2): p. 168.
51. Lee, S.-H., et al., *Effect of heating rate, temperature, and residence time during graphitization on the mechanical and electrical properties of isotropic graphite blocks*. Carbon, 2023. **208**: p. 443-451.
52. Tremel, A., et al., *Experimental investigation of high temperature and high pressure coal gasification*. Applied energy, 2012. **92**: p. 279-285.
53. Farid, M.A.A., et al., *Catalytic graphitization of biomass-derived ethanosolv lignin using Fe, Co, Ni, and Zn: Microstructural and chemical characterization*. Journal of Analytical and Applied Pyrolysis, 2023. **173**: p. 106064.
54. Chen, C., et al., *Catalytic graphitization of cellulose using nickel as catalyst*. BioResources, 2018. **13**(2): p. 3165-3176.
55. Xia, S., et al., *Fe–Co based synergistic catalytic graphitization of biomass: Influence of the catalyst type and the pyrolytic temperature*. Energy, 2022. **239**: p. 122262.

56. Frankenstein, L., et al., *Revealing the Impact of Different Iron - Based Precursors on the 'Catalytic' Graphitization for Synthesis of Anode Materials for Lithium Ion Batteries*. ChemElectroChem, 2023. **10**(5): p. e202201073.
57. Shi, J.-J., et al., *Facile synthesis of iron-and nitrogen-doped porous carbon for selective CO₂ electroreduction*. ACS Applied Nano Materials, 2018. **1**(7): p. 3608-3615.
58. Mohamed, A., et al., *A comparison of the electrochemical performance of graphitized coal prepared by high-temperature heating and flash Joule heating as an anode material for lithium and potassium ion batteries*. Chemical Physics Letters, 2023. **815**: p. 140362.
59. Dreimol, C.H., et al., *Iron - Catalyzed Laser - Induced Graphitization - Multiscale Analysis of the Structural Evolution and Underlying Mechanism*. Small, 2024. **20**(49): p. 2405558.
60. Truong - Phuoc, L., et al., *Induction heating for the electrification of catalytic processes*. ChemSusChem, 2025. **18**(9): p. e202402335.
61. Zhao, X., et al., *Catalytic graphitization of residual carbon from gasification fine slag with ferric chloride as catalyst*. Colloids and Surfaces A: Physicochemical and Engineering Aspects, 2022. **636**: p. 128142.
62. Wang, T., et al., *Catalytic graphitization of anthracite as an anode for lithium-ion batteries*. Energy & Fuels, 2020. **34**(7): p. 8911-8918.
63. Gao, S.W., et al. *Energy consumption and carbon emission analysis of natural graphite anode material for lithium batteries*. in *Materials Science Forum*. 2018. Trans Tech Publ.
64. Dai, Q., et al., *Life cycle analysis of lithium-ion batteries for automotive applications*. Batteries, 2019. **5**(2): p. 48.
65. Shi, Z., et al., *Environmentally friendly valorization of biowaste into high-quality battery graphite within molten metal pool*, K.R.I.o. Technology, Editor. 2025.
66. Pope, C.G., *X-ray diffraction and the Bragg equation*. Journal of chemical education, 1997. **74**(1): p. 129.
67. Cao, H., et al., *Investigation on the mineral catalytic graphitization of anthracite during series high temperature treatment*. Minerals, 2023. **13**(6): p. 749.
68. Naderi, M., *Surface area: brunauer - emmett-teller (BET)*, in *Progress in filtration and separation*. 2015, Elsevier. p. 585-608.
69. Oberacher, H., G. Whitley, and B. Berger, *Evaluation of the sensitivity of the 'Wiley registry of tandem mass spectral data, MSforID' with MS/MS data of the 'NIST/NIH/EPA mass spectral library'*. Journal of Mass Spectrometry, 2013. **48**(4): p. 487-496.

70. Zaini, I.N., et al., *Creating values from biomass pyrolysis in Sweden: Co-production of H₂, biocarbon and bio-oil*. Processes, 2021. **9**(3): p. 415.
71. Wang, Y., et al., *Comparative evaluation of hydrothermal carbonization and low temperature pyrolysis of eucommia ulmoides oliver for the production of solid biofuel*. Scientific reports, 2019. **9**(1): p. 5535.
72. Zaimes, G.G., et al., *Multistage torrefaction and in situ catalytic upgrading to hydrocarbon biofuels: analysis of life cycle energy use and greenhouse gas emissions*. Energy & Environmental Science, 2017. **10**(5): p. 1034-1050.
73. Sandin, G., G.M. Peters, and M. Svanström, *Life cycle assessment of Forest products: challenges and solutions*. Vol. 1. 2016: Springer.
74. Djomo, S.N., et al., *Energy performances of intensive and extensive short rotation cropping systems for woody biomass production in the EU*. Renewable and Sustainable Energy Reviews, 2015. **41**: p. 845-854.
75. Roedl, A., *Production and energetic utilization of wood from short rotation coppice—a life cycle assessment*. The International Journal of Life Cycle Assessment, 2010. **15**(6): p. 567-578.
76. Jones, S., et al., *Process design and economics for the conversion of lignocellulosic biomass to hydrocarbon fuels: fast pyrolysis and hydrotreating bio-oil pathway*. 2013, National Renewable Energy Lab.(NREL), Golden, CO (United States).
77. Zhang, Y., G. Hu, and R.C. Brown, *Life cycle assessment of the production of hydrogen and transportation fuels from corn stover via fast pyrolysis*. Environmental Research Letters, 2013. **8**(2): p. 025001.
78. Rodríguez, F., O. Delgado, and R. Muncrief, *Fuel consumption testing of tractor-trailers in the european union and the united states*. Accessed: May, 2018. **14**: p. 2020.
79. Kantarelis, E., W. Yang, and W. Blasiak, *Production of liquid feedstock from biomass via steam pyrolysis in a fluidized bed reactor*. Energy & fuels, 2013. **27**(8): p. 4748-4759.
80. Vamvuka, D., *Bio - oil, solid and gaseous biofuels from biomass pyrolysis processes—an overview*. International journal of energy research, 2011. **35**(10): p. 835-862.
81. Hu, X., et al., *Coke formation during thermal treatment of bio-oil*. Energy & Fuels, 2020. **34**(7): p. 7863-7914.
82. Dey, S.C., et al., *Catalytic graphitization of pyrolysis oil for anode application in lithium-ion batteries*. Green Chemistry, 2024. **26**(15): p. 8840-8853.

83. Zhang, Y., et al., *Unexpected Structural Effects on the Onset of Thermal Reactions of Aromatic Hydrocarbons*. Energy & Fuels, 2023. **37**(8): p. 5792-5804.
84. Li, Z., et al., *X-ray diffraction patterns of graphite and turbostratic carbon*. Carbon, 2007. **45**(8): p. 1686-1695.
85. Ru, H., et al., *Bean-dreg-derived carbon materials used as superior anode material for lithium-ion batteries*. Electrochimica acta, 2016. **222**: p. 551-560.
86. Wu, X., et al., *Carbon-coated isotropic natural graphite spheres as anode material for lithium-ion batteries*. Ceramics International, 2017. **43**(12): p. 9458-9464.
87. Kim, T., J. Lee, and K.-H. Lee, *Full graphitization of amorphous carbon by microwave heating*. RSC advances, 2016. **6**(29): p. 24667-24674.
88. Ferrari, A.C., *Raman spectroscopy of graphene and graphite: Disorder, electron-phonon coupling, doping and nonadiabatic effects*. Solid state communications, 2007. **143**(1-2): p. 47-57.
89. Jawhari, T., A. Roid, and J. Casado, *Raman spectroscopic characterization of some commercially available carbon black materials*. Carbon, 1995. **33**(11): p. 1561-1565.
90. Ma, W., et al., *Catalytic cracking mechanism of bio-oil model compounds*. Transactions of the Chinese Society of Agricultural Engineering, 2013. **29**(9): p. 207-213.
91. Abou Rjeily, M., et al., *Pyrolysis-catalytic upgrading of bio-oil and pyrolysis-catalytic steam reforming of biogas: a review*. Environmental chemistry letters, 2021. **19**(4): p. 2825-2872.
92. Xia, S., et al., *Reaction kinetics, mechanism, and product analysis of the iron catalytic graphitization of cellulose*. Journal of Cleaner Production, 2021. **329**: p. 129735.
93. Li, Z., et al., *Defective hard carbon anode for Na-ion batteries*. Chemistry of Materials, 2018. **30**(14): p. 4536-4542.
94. Hongtao, L., et al., *Catalytic graphitization of coke carbon by iron: Understanding the evolution of carbon Structure, morphology and lattice fringes*. Fuel, 2020. **279**: p. 118531.
95. Rios, C.d.M.S., et al., *Biochars from various biomass types as precursors for hard carbon anodes in sodium-ion batteries*. Biomass and Bioenergy, 2018. **117**: p. 32-37.
96. Shigapov, A.N., et al., *The preparation of high-surface-area cordierite monolith by acid treatment*. Applied Catalysis A: General, 1999. **182**(1): p. 137-146.

97. Ng, S., et al., *Correlations between surface properties of graphite and the first cycle specific charge loss in lithium-ion batteries*. Carbon, 2009. **47**(3): p. 705-712.
98. Ōya, A. and H. Marsh, *Phenomena of catalytic graphitization*. Journal of Materials Science, 1982. **17**(2): p. 309-322.
99. Agubra, V.A. and J.W. Fergus, *The formation and stability of the solid electrolyte interface on the graphite anode*. Journal of Power Sources, 2014. **268**: p. 153-162.
100. Hatzikraniotis, E., C. Mitsas, and D. Siapkias, *Differential capacity analysis, a tool to examine the performance of graphites for Li-ion cells*, in *Materials for Lithium-Ion Batteries*. 2000, Springer. p. 529-534.
101. Rowden, B. and N. Garcia-Araez, *Estimating lithium-ion battery behavior from half-cell data*. Energy Reports, 2021. **7**: p. 97-103.
102. Engels, P., et al., *Life cycle assessment of natural graphite production for lithium-ion battery anodes based on industrial primary data*. Journal of Cleaner Production, 2022. **336**: p. 130474.